INFORMATION TO USERS

This manuscript has been reproduced from the microfilm master. UMI films the text directly from the original or copy submitted. Thus, some thesis and dissertation copies are in typewriter face, while others may be from any type of computer printer.

The quality of this reproduction is dependent upon the quality of the copy submitted. Broken or indistinct print, colored or poor quality illustrations and photographs, print bleedthrough, substandard margins, and improper alignment can adversely affect reproduction.

In the unlikely event that the author did not send UMI a complete manuscript and there are missing pages, these will be noted. Also, if unauthorized copyright material had to be removed, a note will indicate the deletion.

Oversize materials (e.g., maps, drawings, charts) are reproduced by sectioning the original, beginning at the upper left-hand corner and continuing from left to right in equal sections with small overlaps. Each original is also photographed in one exposure and is included in reduced form at the back of the book.

Photographs included in the original manuscript have been reproduced xerographically in this copy. Higher quality 6" x 9" black and white photographic prints are available for any photographs or illustrations appearing in this copy for an additional charge. Contact UMI directly to order.

UMI®

University of Alberta

Passive and Electrooptic Polymer Photonic Devices

by

David Weldon Boertjes ©

A thesis submitted to the Faculty of Graduate Studies and Research in partial fulfillment
of the requirements for the degree Doctor of Philosophy.

Department of Electrical and Computer Engineering

Edmonton, Alberta

Spring, 1999

Canada

<div align="center">

University of Alberta

Library Release Form

</div>

Name of Author: David Weldon Boertjes
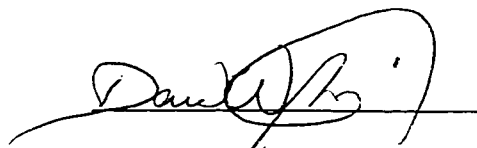
Title of Thesis: Passive and Electrooptic Polymer Photonic Devices

Degree: Doctor of Philosophy

Year this Degree Granted: 1999

Permission is hereby granted to the University of Alberta Library to reproduce single copies of this thesis and to lend or sell such copies for private, scholarly, or scientific research purposes only.

The Author reserves all other publication and other rights in association with the copyright in the thesis, and except as hereinbefore provided, neither the thesis nor any substantial portion thereof may be printed or otherwise reproduced in any form whatever without the author's prior written permission.
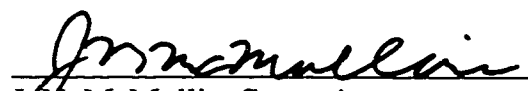
477 Terrace Street,
New Glasgow, NS B2H 5J6

Date: _October 23, 1998_
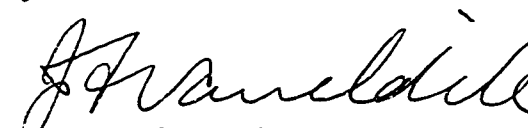
University of Alberta

Faculty of Graduate Studies and Research

The undersigned certify that they have read, and recommend to the Faculty of Graduate Studies and Research for acceptance, a thesis entitled Passive and Electrooptic Polymer Photonic Devices by David Weldon Boertjes in partial fulfillment of the requirements for the degree of Doctor of Philosophy.

J. N. McMullin, Supervisor

J. F. Vaneldik

F. E. Vermeulen

S. K. Dew

J. L. Pinfold

D. Irvine-Halliday, External Examiner

Date: _Oct. 22, 1998_

to my family

Abstract

Polymeric materials are of great interest in current photonic research for reasons of cost and versatility. This thesis presents a collection of work in three research topics that are unified through the use of polymers in photonic devices. The topics covered are: a unique formulation of the beam propagation method for the accurate simulation of waveguide bends; the analysis of a novel graded effective index polymer waveguide structure; and the design, fabrication and testing of a 2X2 polymer electrooptic modulator/switch.

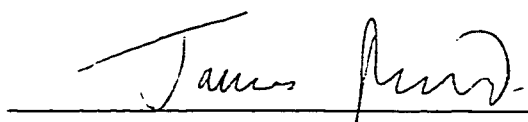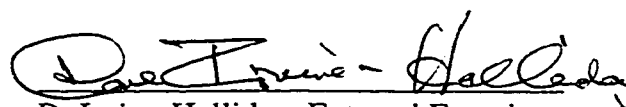The beam propagation method described is a three-dimensional simulation tool whose novel aspect is the retention of the full form of the wave equation in cylindrical coordinates. The result is an increase in the predicted losses of bent waveguides over the methods previously reported, which are significant for bending radii much less than one millimeter. Previous methods make simplifying approximations that are only valid for large radii of curvature.

The graded effective index planar polymer waveguides presented are novel structures that have not been previously analyzed. The theory and subsequent simulations of the structures match well to the experiments that were performed, and, having no free parameters, demonstrate that the underlying phenomenon is well understood. Applications of these waveguides are proposed in coarse wavelength division multiplexing and waveguide optical amplifiers. Both of these applications employ the useful capability of these structures to tailor waveguide dispersion to offset material dispersion.

The design and fabrication of a novel polymer electrooptic modulator/switch is presented herein. The device employs a unique combination of optical materials, namely, fused silica and electrooptic polymer. The electrical portion of the device uses coplanar waveguide electrodes to both pole and drive the device. The device geometry is novel in that the coplanar waveguides are velocity matched to the optical waveguides creating a travelling wave modulator. Optical loss in the fabricated devices was high (>60dB) due to problems in the fabrication process. Modulation was measurable only at low frequencies because of the high optical loss; however, electrical measurements suggest that the devices would meet the design criterion for modulation bandwidth, being able to transmit >10Gb/s signals.

Acknowledgments

I would like to first acknowledge the support and guidance of Dr. J. N. McMullin as my supervisor, mentor, and friend. Next I will thank the members of the Photonics group at TRLabs past and present. C. W. Unick, M. Krishnaswamy, R. Nagarajan, M. R. Paiam, S. Walklin, D. D. Clegg, A. J. P. Hnatiw, D. J. Corazza, R. I. MacDonald, B. P. Keyworth and others all of whom have undoubtedly made contributions to this work through knowledge amassed in the group shared freely through countless conversations. I would also like to thank C. W. Unick for providing Matlab code that facilitated the timely layout of photolithographic masks.

Table of Contents

List of Tables

List of Figures

List of Symbols

a	core radius of an optical fibre
A	modulation amplitude
α	attenuation factor
α_e	electrical decay constant
α_m	decay constant of the mth slab mode in the substrate material
α_{min}	the minimum value which the attenuation factor, α, may attain
β_m	longitudinal propagation constant of the mth mode
c	speed of light in a vacuum
C	capacitance
d_x	x offset of an input field
d_y	y offset of an input field
$\hat{D}$	diffraction operator
$\hat{\tilde{D}}$	Fourier transformed diffraction operator
δ	modulation depth
Δ	modifier indicating a small change in the variable which follows
∇^2	Laplacian differential operator
e	the natural number
E	electric field
E_m	x and z dependent electric field distribution of the mth slab mode
E_o	initial field amplitude
ε	electrical permittivity
$\varepsilon_{\textit{eff}}$	effective relative electrical permittivity
ε_r	relative electrical permittivity
$\mathcal{F}$	Fourier transform
$\mathcal{F}^{-1}$	inverse Fourier transform
F	modified E-field
γ_m	decay constant of the mth slab mode in the cladding material

Γ	waveguide confinement factor
h	height of a waveguide structure
i	the imaginary number
I_i	input light intensity
I_o	output light intensity
k_1	propagation constant of light in a medium having refractive index n_1
k_e	propagation constant of an electrical signal
k_o	free-space propagation constant of light
K_m	vertical propagation constant of the mth slab mode
L	length
L_c	conductor length of microwave coplanar waveguide
L_{MMI}	length of a multimode interference coupler
L_π	characteristic imaging length of a multimode interference coupler
λ	wavelength
m	mode number
n	index of refraction
$\hat{n}$	outward pointing unit normal
n_{eff}	effective index
n_{elec}	effective index of an electrical signal
n_m	graded effective index of the mth slab mode
n_{opt}	effective index of an optical signal
N_m	arbitrary normalization constant for the mth slab mode
NX	number of points in a grid along the x-axis
NY	number of points in a grid along the y-axis
$O[x^n]$	terms of order x^n
ω_e	angular frequency of an electrical signal
$\overline{P}$	average electrical power
π	pi, ratio of the circumference to the diameter of a circle
q	replacement variable used in Fourier transforms

θ	angular coordinate in a cylindrical coordinate system
θ_e	arbitrary phase constant used for an electrical signal
r	radial coordinate in a cylindrical coordinate system
r_{ij}	linear electrooptic coefficients
R	radius of curvature
$\hat{R}$	refraction operator
s_c	gap size between conductors in microwave coplanar waveguide
S_m	modes of a slab waveguide
σ	Gaussian beam size
t	time
t_c	conductor thickness
τ	period
u	transformed variable to replace r
v_e	velocity of an electrical signal
v_o	velocity of an optical signal
V	voltage
V_π	voltage needed to produce a π phase change
w	width of a waveguide structure
w_c	center conductor width in microwave coplanar waveguide
W	width of a multimode interference coupler
$\hat{W}$	refraction operator in transformed coordinates
W_e	effective width of a multimode interference coupler
x	one of three orthogonal coordinates in a Cartesian coordinate system, or the third axis in a cylindrical coordinate system along with r and θ
$\hat{X}$	secondary diffraction operator in transformed coordinates
$\hat{\tilde{X}}$	Fourier transformed secondary diffraction operator in transformed coordinates
y	one of three orthogonal coordinates in a Cartesian coordinate system
z	one of three orthogonal coordinates in a Cartesian coordinate system
Z_c	characteristic impedance
∞	infinity

List of Abbreviations

2D	two dimensional
3D	three dimensional
AC	alternating current
BPM	beam propagation method
BW	bandwidth
CPW	coplanar waveguide
CT	coordinate transform
DC	direct current
DPL	differential power loss
DR1	disperse red 1
EDFA	erbium-doped fibre amplifier
EO	electrooptic
FD	finite difference
FFT	fast Fourier transform
Gb/s	gigabit per second
GRIN	graded index
IM	index modification
MM	multimode
MMI	multimode interference
NOA	Norland optical adhesive
PMMA	poly(methylmethacrylate)
POEMS	polymer electrooptic modulator switch
RIE	reactive ion etching
SM	singlemode
TEM	transverse electric-magnetic
TL	transition loss
UV	ultraviolet

1. Introduction

The world we live in requires communication on many levels, the most basic of which is human-to-human. Indeed the invention of the telegraph and the telephone were answers to this need that irrevocably changed our world and resulted in the creation of widespread telecommunications networks. A similar revolution has occurred in electronic computing devices that has resulted in the need for communications from computer-to-computer. Today, these needs are echoed in the demand for higher bandwidth telecommunications and similarly in computing as a demand for higher processing speeds.

Light is undoubtedly a most attractive means for communication. The photons of which light is comprised do not readily interact with each other except by means of an intervening particle, and therefore, to a large degree, are immune to the effects of electromagnetic interference. The invention of optical fibres has revolutionized telecommunications and their potential bandwidth is only now beginning to be exploited. Wavelength Division Multiplexing (WDM) is a maturing technology that allows multiple wavelength channels to be carried on a single fibre span. Optical amplification is another technology that is expanding the capability of fibre optic networks. Maximizing the speed of transmission and the number of wavelength channels carried on a fibre is a step along the way to full utilization of the existing fibre base and a response to the increasing demand for network bandwidth.

Computing devices too may experience a revolution in the near future as processing speeds place higher demands on conventional electronics. Communications inside a computer on a board-to-board or perhaps a chip-to-chip level may benefit from the implementation of optical interconnection, because, as frequency increases electrical interconnections experience higher losses and crosstalk [1]. Optical interconnection

1

provides a means to achieve the same function while consuming less power which alleviates some of the problems of heat dissipation in integrated circuits. In addition, the higher integration densities can be achieved in optical interconnects because of the reduced electromagnetic coupling between adjacent channels compared to electrical connections. For these reasons, photonic devices are under intense research for application in computing devices.

Optical devices implemented in planar structures are of current interest in photonics research. Planar waveguides are attractive, as they are compatible with integration into conventional electronics. Many levels of integration can be identified: monolithic integration combines optical waveguides and electronic components in the same semiconductor material system; hybrid integration employs different materials for the optical and electronic devices which are integrated onto a single substrate; and integrated optics incorporates the necessary waveguide structures onto a single substrate to perform some optical function. The types of devices integrated into these structures can be divided by function into the categories passive and active. For example, passive waveguide devices provide such functions as power splitters/combiners, filters, etc. Active devices, sometimes termed integrated optoelectronic devices, include modulators, switches, amplifiers, etc. Having a framework for the applications of photonics, it is then important to develop tools for the efficient design and simulation of the types of structures used in such devices.

1.1. The Beam Propagation Method

One aspect in the design of photonic devices is the prediction of the optical fields throughout the waveguide structures. Properties such as losses, phase information, mode distributions, etc. must be ascertained in order to predict the performance of a device. The Beam Propagation Method (BPM) is the tool of choice for the simulation of optical

2

waveguides. Figure 1.1 shows a schematic of the type of problem which can be solved using the BPM. The structure shown is a dielectric optical waveguide in which the propagation of light will be dominantly in the z-direction. The method used a step-wise approach which "propagates" the solution from calculation plane to calculation plane. A known light distribution, or in particular electric field distribution, is the starting point introduced on the first calculation plane on the left-hand side. This known "solution" is then used to find the solution on the next calculation plane a distance Δz away. In this way, the method is computationally efficient as it only needs to work on a single calculation plane at a time which drastically reduces the amount of storage needed as compared to methods which must store the entire calculation volume, i.e. all planes along z.

calculation planes

propagation direction
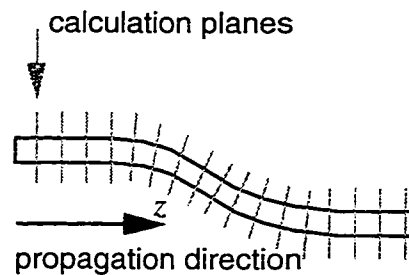
Figure 1.1: An example of a simulation which could be performed by the BPM. The light enters the structure on the left-hand side and is "propagated" in a step-wise manner through the structure using the solution from the previous calculation plane to obtain the solution on the following calculation plane.

A problem of particular interest for integrated optic devices is that of bent waveguides. In order to fabricate devices in the smallest space possible it is often necessary to use bent waveguides. The minimum radius of curvature that can be tolerated depends on the waveguide structure and the acceptable loss for propagation through the structure. Chapter 2 presents a novel formulation of the BPM that is implemented in cylindrical coordinates which is therefore able to model waveguide bends. In addition, by introducing a variable radius of curvature, which is made to match the local radius of curvature of a waveguide structure, the BPM can model arbitrarily

3

bent planar waveguide structures as the concatenation of small circular arcs. The described method is unique in that it retains the full form of the scalar wave equation unlike the methods that have been reported previously.

1.2. Planar Polymer Waveguides

As mentioned previously, optical waveguides have applications as interconnects for electrical components. In particular, step index multimode (MM) waveguides have been extensively researched for this purpose as they are easy to fabricate, exhibit low loss and have good coupling properties to sources and detectors. For board-to-board scale interconnects, where propagation distances can be on the order of a meter, dispersion may limit the bandwidth (BW) of the optical connection.

In the early days of optical fibre, before the widespread use of singlemode (SM) fibres, graded index fibre was employed to reduce the dispersion penalty associated with step-index structures. In fibre with the appropriate gradation of the index, the dispersion can be reduced by three orders of magnitude when compared to a step-index structure of similar dimensions. In Chapter 3 a novel type of waveguide structure which exhibits graded index behaviour is presented [2]. This structure has the potential to increase the BW of board-to-board scale interconnects in the same way as graded index optical fibre has increased the BW of multimode fibres.
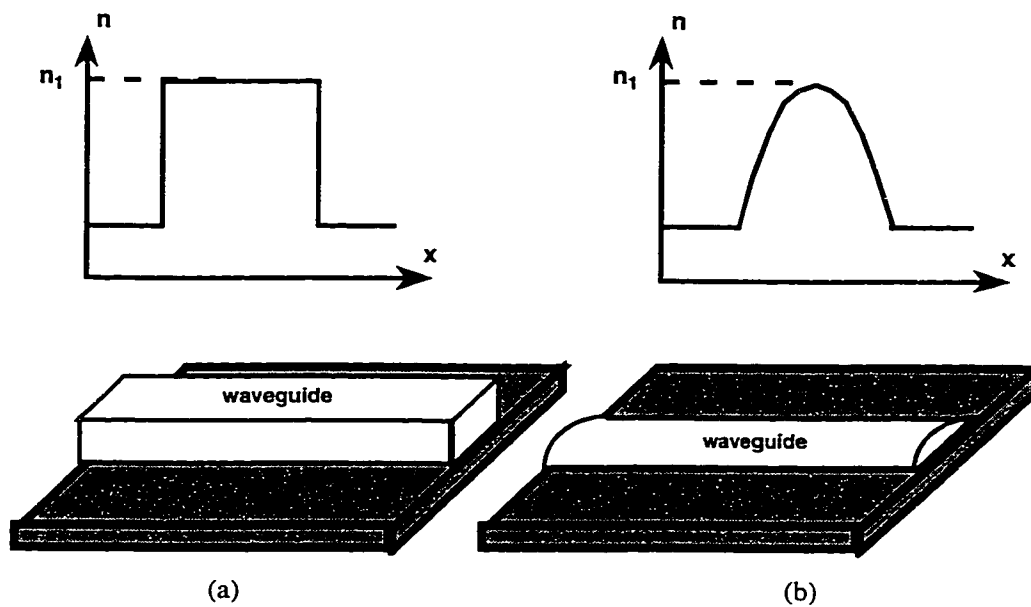
Figure 1.2: (a) top: typical step-index profile and bottom: corresponding realization in a planar waveguide. (b) top: typical graded-index profile and bottom: corresponding realization in a planar waveguide.

Figure 1.2 shows a schematic representation of the two types of MM waveguide. The curved boundary of the waveguide shown in Figure 1.2(b) tends to confine the light to the center of the waveguide in a way similar to the effect of a graded index in an optical fibre. Since these waveguides were fabricated in polymer, they have been termed graded effective index planar polymer waveguides. The applications of these waveguides are not only in interconnects but also have been identified in coarse WDM and waveguide optical amplifiers.

1.3. Electrooptic Polymers

Polymeric materials are currently the focus of a great deal of photonic device research. Among the reasons for this is their intrinsic versatility. They can be cast into shapes that may be difficult to achieve in other optical materials. Another attraction to polymers is cost. Not only does polymer often cost less than other optical materials but also the patterning of the polymer is compatible with standard photolithographic

techniques. Polymers can also be functionalized through the addition of active components that permit the material to exhibit a wanted effect such as the modulation of light intensity with the application of an electric field, i.e. the electrooptic effect. A polymer can be made electrooptic through the addition of an organic dye molecule.

Chapter 4 details the design, fabrication and testing of a novel electrooptic polymer device. An electrooptic polymer is used to form a generalized Mach-Zehnder waveguide interferometer that has two inputs and two outputs. The switching function is achieved using voltages applied to gold electrodes fabricated in the form of microwave coplanar waveguides. The velocities of the signals on the electrical and optical waveguides are then matched to achieve high BW.

This device has direct application to telecommunications as an external modulator. The high-speed signals needed in transmission networks can prohibit the use of direct current modulation of a laser diode. Even when it is possible to use this form of modulation, it is often the case that a better modulated optical signal is obtained by using an external modulator. The external modulation also allows the laser to operate in a constant current mode which improves the stability and extends the lifetime of the device. Stability, especially of the emitted wavelength, is increasingly important as WDM systems compress more channels into the relatively small wavelength window offered by Erbium-Doped Fibre Amplifiers (EDFAs).

2. The Coordinate Transform Beam Propagation Method

2.1. Introduction to the Beam Propagation Method

The beam propagation method (BPM) has become one of the most popular tools for the design and analysis of integrated optical devices. The method was first developed using a split-step fast Fourier transform technique (FFT-BPM) to solve the scalar wave equation and was applied to graded index optical fibres [3]. Since then, many modifications to this algorithm have been made, such as the finite difference BPM (FD-BPM) which allows semi- [4] and full- [5] vectorial formulations, and the application of transparent boundary conditions [6]. Vectorial FD-BPMs have been implemented in 3D simulations. However, this extension is simple only for the paraxial approximation. Even wide-angle propagators, which require no extra computation in the FFT-BPM, become cumbersome in 3D FD simulations. These problems are usually overcome by using a series expansion of the propagator, the terms of which are applied in succession. Even for modest sized grids (with NX by NY points), 3D FD-BPMs require the solution of a matrix equation containing $(NX*NY)^2$ elements which is best handled using sparse matrix linear algebra. After considering these complications, the computation time advantage of FD-BPMs for 3D simulations is all but lost.

There are also classes of problems well suited to the FFT-BPM; i.e. structures having small index differences [7]. For example, there are material systems which are currently being investigated for use in integrated optics, such as glasses and polymers, which, when used to construct singlemode waveguides typically have index variations of only a few percent [8]. In addition, the design of integrated optical devices usually

7

employs bent waveguides. It is therefore important to model the propagation characteristics of these bends, such as losses and mode shapes.

The problem of bent waveguides has been treated in numerous ways. Many non-BPM analyses have focused on slab waveguides (2D case) [9-11] while others have concentrated on a particular geometry of interest such as optical fibres [12-14]. The simplest method of including a radius of curvature in a BPM is to transform a curved waveguide into an equivalent straight waveguide by introducing a modified refractive index profile. This method has been applied in 2D simulations resulting in an Index Modification-BPM (IM-BPM) [15-18]. Other 2D BPMs have departed from the IM-BPM by using methods such as: a rotating grid at each step [19], the Galerkin method in polar coordinates [20], or finite differences in polar coordinates [21]. 3D IM-BPMs have been demonstrated using paraxial [22,23] and wide-angle propagators [24]. The method of lines has also been applied to 3D modeling of curved waveguides [25].

In this chapter, an adaptation of the 3D wide-angle FFT-BPM to cylindrical polar coordinates is presented. In addition, by introducing a continuously variable radius of curvature, the grid is allowed to follow arbitrary paths.

2.2. Simulation Model

2.2.1 FFT-BPM in Cylindrical Coordinates

The usual starting point to derive the FFT-BPM is the scalar wave equation,

$$\left[r \frac{\partial}{\partial r} \left(r \frac{\partial}{\partial r} \right) + \frac{\partial^2}{\partial \theta^2} + r^2 \frac{\partial^2}{\partial x^2} + r^2 k_o^2 n^2 \right] E = 0 , \qquad (2.1)$$

given here in cylindrical coordinates where n is the index of refraction and $k_o = 2\pi / \lambda$. It is convenient to set up a local coordinate system for the computation space of the BPM, a

8

distance R from the origin along the r axis (see Figure 2.1). Therefore, let $r = y + R$ and $z = R\theta$.
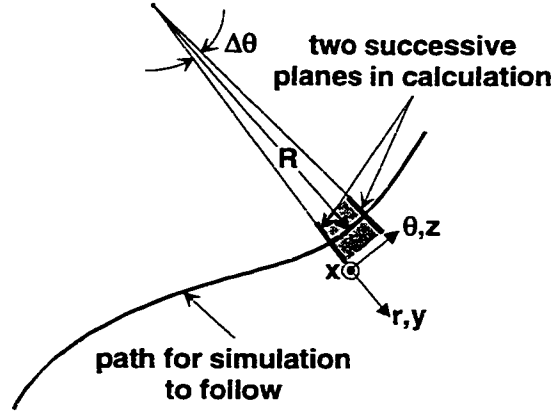
Figure 2.1: An example of an arbitrary path for the simulation to follow. The shaded area shows the calculation window for a single step in the propagation. The local coordinate system, shown to the side of this area, is centered on the centerline path.

In two dimensions, it is possible to find a conformal mapping which transforms the polar wave equation into a Cartesian-like wave equation for which the form of the BPM is well known [10]. This is equivalent to the coordinate transformations:

$$u = R \ln(r / R) \tag{2.2a}$$

$$z = R\theta. \tag{2.2b}$$

Using the same coordinate transformations in the 3D case, equation (2.1) can be rewritten as

$$\left[\frac{\partial^2}{\partial z^2} + \frac{\partial^2}{\partial u^2} + \frac{\partial^2}{\partial x^2} + \left(e^{\frac{2u}{R}} - 1 \right) \frac{\partial^2}{\partial x^2} + k_o^2 e^{\frac{2u}{R}} n^2 \right] E = 0. \tag{2.3}$$

This equation has the same form as the Cartesian wave equation with the exception of an extra factor, $\exp(2u / R)$, in front of the index of refraction, and an extra term, $[\exp(2u / R) - 1]\partial^2 / \partial x^2$. This extra term is dropped in the IM-BPM and the approximation $u \approx y$ is made which is only valid for large radii of curvature. The extra factor, $\exp(2u / R)$, is then taken together with the index of refraction to create a modified index profile.

9
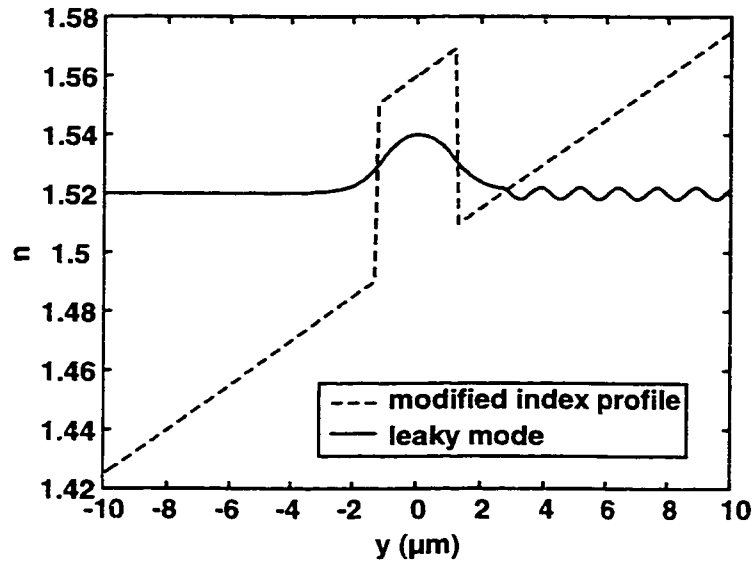
Figure 2.2: Schematic representation of the effect of curvature on the mode in a waveguide. The dashed line is the modified index profile which results from the bending radius, and the solid line represents the electric field of a mode. This mode experiences a loss due to radiation (shown as the sinusoidal portion) leaking out of the guide into the higher index region.

Figure 2.2 shows a schematic representation of the effect of curvature on the modified index profile of a waveguide and the resulting leaky mode which loses light to radiation on the outside of the bend.

The method described herein differs from the IM-BPM in that it retains the full form of (2.3) to derive a Coordinate Transform BPM (CT-BPM). The assumed equation given below can be shown to be consistent with equation (2.3) and is the form necessary for use in a BPM algorithm:

$$\frac{\partial E}{\partial z} = -i\sqrt{\hat{D} + \hat{R}}\, E \tag{2.4}$$

where the choice of sign implies that one direction of propagation has been assumed and

$$\hat{D} = \frac{\partial^2}{\partial u^2} + \frac{\partial^2}{\partial x^2} + k_I^2 \tag{2.5a}$$

$$\hat{R} = \hat{W} + \hat{X} \tag{2.5b}$$

and

$$\hat{W} = k_o^2 \left(e^{\frac{2u}{R}} n^2 - n_1^2 \right)$$ (2.5c)

$$\hat{X} = \left(e^{\frac{2u}{R}} - 1 \right) \frac{\partial^2}{\partial x^2}.$$ (2.5d)

A uniform background index, n_1, has been chosen where $k_1 = k_o n_1$. $\hat{D}$ is the usual

diffraction operator and $\hat{R}$ is our new refraction operator. $\hat{R}$ is composed of two parts,

$\hat{W}$ and $\hat{X}$, where $\hat{W}$ is the usual refraction operator with a modified index of refraction

$\hat{X}$ is an extra diffraction operator, acting in only the x-direction, which accounts for the

increased size of the grid cells as u increases. The conventional $\hat{R}$ of the split-step FFT-

BPM is regained as $R \rightarrow \infty$ (straight propagation). Following the usual approach, the

formal solution to (2.4) is

$$E(z + \Delta z) = \exp(-i\sqrt{\hat{D} + \hat{R}}\,\Delta z)E(z),$$ (2.6)

where the exponential is called a propagator because, through its application, it

"propagates" the solution from one plane in z to the next. The square root can be

expanded in the approximate form

$$\sqrt{\hat{D} + \hat{R}} = \sqrt{\hat{D}} + \frac{\hat{R}}{2k_1}$$
$$= \sqrt{\hat{D}} + \frac{\hat{W}}{2k_1} + \frac{\hat{X}}{2k_1}$$ (2.7)

The problem at this point is to find a way of finding the solution, (2.6), in steps using

(2.7). In the conventional FFT-BPM, it is recognized that the $\hat{D}$ operator is diagonal in

Fourier space and the $\hat{R}$ operator is diagonal in real space. Since the two do not

commute, the splitting of steps is done in the following way:

$$\exp\left[\left(\sqrt{\hat{D}} + \frac{\hat{R}}{2k_1} \right) \Delta z \right] = \exp\left[\sqrt{\hat{D}} \frac{\Delta z}{2} \right] \exp\left[\frac{\hat{R}}{2k_1} \Delta z \right] \exp\left[\sqrt{\hat{D}} \frac{\Delta z}{2} \right] + O[\Delta z^3].$$ (2.8)

11

The repeated application of (2.8), to propagate through multiple steps, allows the collapse of two half steps of diffraction for each step in z; this is the classic split-step FFT-BPM [3].

The final form of (2.7) has three operators, thus, an expansion similar to (2.8) must be found:

$$\exp\left[-i\left(\sqrt{\hat{D}}+\frac{\hat{W}}{2k_1}+\frac{\hat{X}}{2k_1}\right)\Delta z\right]=\exp\left[-i\sqrt{\hat{D}}\frac{\Delta z}{2}\right]\exp\left[-i\frac{\hat{X}}{2k_1}\frac{\Delta z}{2}\right]\exp\left[-i\frac{\hat{W}}{2k_1}\Delta z\right]$$
$$\times\exp\left[-i\frac{\hat{X}}{2k_1}\frac{\Delta z}{2}\right]\exp\left[-i\sqrt{\hat{D}}\frac{\Delta z}{2}\right]+O\left[\Delta z^3\right]$$

.(2.9)

There are two advantages to this order of expansion. Firstly, the original propagation formula, (2.8), is regained directly for straight propagation. Secondly, the $\hat{X}$ operator requires only one-dimensional FFTs (and inverse FFTs) and is therefore best applied adjacent to the $\hat{D}$ operator which is applied in Fourier space. To see the benefit of this expansion, it is useful to show how the transforms fit into the evaluation of a single step;

$$\mathcal{F}_{x,y}^{-1}\exp\left[-i\sqrt{\hat{\tilde{D}}}\frac{\Delta z}{2}\right]\mathcal{F}_y\exp\left[-i\frac{\hat{\tilde{X}}}{2k_1}\frac{\Delta z}{2}\right]\mathcal{F}_x\exp\left[-i\frac{\hat{W}}{2k_1}\Delta z\right]$$
$$\times\mathcal{F}_x^{-1}\exp\left[-i\frac{\hat{\tilde{X}}}{2k_1}\frac{\Delta z}{2}\right]\mathcal{F}_y^{-1}\exp\left[-i\sqrt{\hat{\tilde{D}}}\frac{\Delta z}{2}\right]\mathcal{F}_{x,y}$$

(2.10)

where $\mathcal{F}$ denotes the forward and reverse Fourier transforms with respect to the specified variables, and the tilde on an operator indicates that it has been appropriately transformed. Repeated application in the main loop of the program, allows the cancellation of the two 2D transforms and the collapse of the two half steps of diffraction into a single full step. When using the row-column method to perform the 2D FFTs, this algorithm devotes the same number of computation steps to the FFTs as does the classic BPM (inside the main loop). The only extra computations are the multiplications needed for the application of the $\hat{\tilde{X}}$ operators (for constant radius bends).

12

2.2.2 Derivation of the Propagator

An electric field defined at a point, z, on a plane perpendicular to the direction of propagation, can be propagated through a step of Δz using (2.9)

$$E(z + \Delta z) = \exp\left[-i\sqrt{\hat{D}}\,\frac{\Delta z}{2}\right]\exp\left[-i\frac{\hat{X}}{2k_1}\frac{\Delta z}{2}\right]\exp\left[-i\frac{\hat{W}}{2k_1}\Delta z\right]$$
$$\times \exp\left[-i\frac{\hat{X}}{2k_1}\frac{\Delta z}{2}\right]\exp\left[-i\sqrt{\hat{D}}\,\frac{\Delta z}{2}\right]E(z) \tag{2.11}$$

The form of each of the operators must be found starting with the diffraction operator, along with which the slowly varying envelope approximation is applied, i.e.

$$E(z) = \exp[-ik_1 z]F(z) \tag{2.12}$$

and

$$E(z + \Delta z) = \exp[-ik_1(z + \Delta z)]F(z + \Delta z), \tag{2.13}$$

where F is like the E-field but with the fast variation removed. Applying a full step of diffraction using (2.5a) to E and substituting F, the exponential can be written

$$\exp\left[i\Delta z\left(\frac{-\nabla_t^2}{k_1 + \sqrt{\nabla_t^2 + k_1^2}}\right)\right] \tag{2.14}$$

where

$$\nabla_t^2 = \frac{\partial^2}{\partial u^2} + \frac{\partial^2}{\partial x^2}. \tag{2.15}$$

By taking a 2D Fourier transform, $\nabla_t^2 \rightarrow -q_t^2$, where $\bar{q}_t$ is the variable used in the transform to replace $\bar{r}_t$ (the position vector in the x-u plane). Then a full step of diffraction is evaluated (in Fourier space) as the following:

$$\exp\left[i\Delta z\left(\frac{q_t^2}{k_1 + \sqrt{k_1^2 - q_t^2}}\right)\right]. \tag{2.16}$$

A full step of refraction using (2.5c) is similarly applied (in real space) as:

13

$$\exp\left[i\frac{k_o\Delta z}{2n_1}\left(n_1^2 - e^{\frac{2u}{R}}n^2\right)\right].$$ (2.17)

The $\hat{X}$ operator from (2.5d) also requires the use of the Fourier transform, though only in one dimension, having the effect of replacing $\partial^2/\partial x^2$ with $-q_x^2$. Thus, a full step of x-diffraction is applied (in x-Fourier, u-real space) as:

$$\exp\left[i\frac{\Delta z}{2k_1}\left(e^{\frac{2u}{R}} - 1\right)q_x^2\right].$$ (2.18)

2.3. Numerical Implementation

The BPM is evaluated on a 3D grid, which is able to follow an arbitrary path, such as that of a curved waveguide. This is achieved in two steps; first, a centerline path is defined, and second, the cross-sectional refractive index profile at each point is determined. The path is used to find the local radius of curvature, R. As R changes so does the spacing of u along y. For each step R is changed, the E-field is interpolated onto the new grid using a cubic spline.

The Fourier transforms used in the derivation of (2.16) and (2.18) are implemented using the fast Fourier transform (FFT) algorithm. The effect of discretizing the transform must be considered, and can be lessened by substituting:

$$q_t^2 \rightarrow \tilde{q}_t^2 = \tilde{q}_x^2 + \tilde{q}_u^2 = \left(\frac{2}{\Delta x}\right)^2 \sin^2\left(\frac{q_x\Delta x}{2}\right) + \left(\frac{2}{\Delta u}\right)^2 \sin^2\left(\frac{q_u\Delta u}{2}\right)$$ (2.19)

in all previous expressions [26].

The cyclic nature of the FFT causes fields leaving the simulation window through one side of the grid to reenter on the opposite side. Absorbing boundary conditions are used to remove this unwanted radiation from the calculation area. The following simulations used a raised cosine absorber function, α, defined as [24]

14

$$\alpha(x,y) = \begin{cases} \dfrac{1-\alpha_{min}}{2}\left\{1+\cos\left[\pi\left(\dfrac{y_{a1}-y}{y_{a1}-y_{min}}\right)^3\right]\right\}+\alpha_{min} & \text{area 1} \\[2em] \dfrac{1-\alpha_{min}}{2}\left\{1+\cos\left[\pi\left(\dfrac{x-x_{a2}}{x_{max}-x_{a2}}\right)^3\right]\right\}+\alpha_{min} & \text{area 2} \\[2em] \dfrac{1-\alpha_{min}}{2}\left\{1+\cos\left[\pi\left(\dfrac{y-y_{a2}}{y_{max}-y_{a2}}\right)^3\right]\right\}+\alpha_{min} & \text{area 3} \\[2em] \dfrac{1-\alpha_{min}}{2}\left\{1+\cos\left[\pi\left(\dfrac{x_{a1}-x}{x_{a1}-x_{min}}\right)^3\right]\right\}+\alpha_{min} & \text{area 4} \\[2em] 1 & \text{area 5} \end{cases} \qquad (2.20)$$

where α_{min} is the smallest value α may attain, $x_{a1}, x_{a2}, y_{a1}, y_{a2}, x_{min}, x_{max}, y_{min}$, and y_{max} are boundaries for the grid and the absorber as shown in Figure 2.3. At each step the E-field is multiplied by this matrix to achieve the proper attenuation.
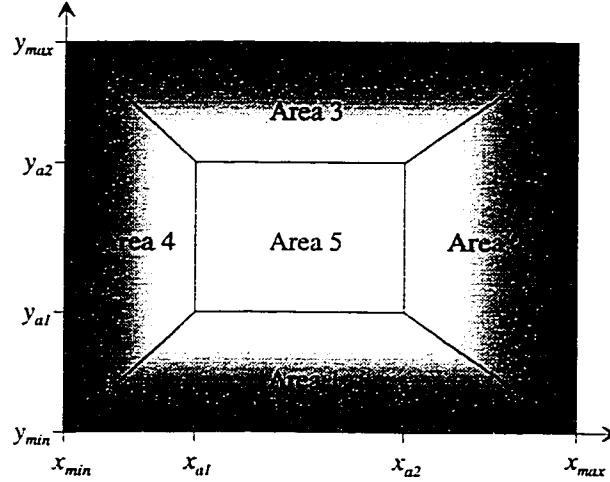
Figure 2.3: Geometry of the absorber used to eliminate radiated fields. The darker the shading, the higher the attenuation.

Since the BPM will be used in the calculation of losses, numerical attenuation (or gain) must be minimized. The source of numerical loss in the FFT-BPM is the wide-angle diffraction operator, as given in equation (2.16). When small transverse grid spacings are chosen, $\tilde{q}_t$ can be greater than k_1 for a portion of the grid, causing the square root in (2.16) to become imaginary. This introduces an artificial loss into the calculation. The simplest method to correct for this loss is to perform a renormalization

15

of the diffraction step. For numerical efficiency, a renormalization factor is accumulated over many steps and applied later. Since the other operators are unitary (for the simulation of lossless structures, i.e. n is real), this method ensures conservation of power. Note also that this renormalization is applied in the implementation of the IM-BPM for the simulations described in the following section.

It is important to note that the split-step BPM algorithm has an advantage over FD methods for the elimination of numerical attenuation in that the source of this attenuation can be uniquely identified. Although renormalization could be used in a FD algorithm it would be difficult to differentiate between power loss due to material absorption (included through a complex refractive index), light exiting the calculation window (using transparent boundary conditions) and unwanted numerical loss. The split-step method differs since the contributions of material loss or gain and the absorbing boundary conditions are applied in the refraction step, the operator for which contains no unwanted numerical loss. Only the diffraction operator is problematic and the diffraction step is applied in "free space" of a uniform background refractive index. This step is separated from any material properties or boundary conditions and can be renormalized to guarantee the elimination of numerical loss for the entire method.

2.4. Results

2.4.1 Bent fibre

This section presents previously published simulations of bent fibre [24] recalculated here for comparison to the CT-BPM. The fibre is singlemoded at the simulation wavelength, $\lambda = 1.55\,\mu m$, having a core radius, $a = 5\,\mu m$, and refractive indices of 1.503 and 1.500 for the core and cladding areas respectively. The calculation window has 128x128 points and grid spacing $\Delta x = \Delta u = 0.833\,\mu m$. Each step in the

propagation direction is of length $\Delta z = 0.2\,\mu m$. The fibre considered is the concatenation of straight and bent sections, where the bends are of constant radius of curvature, R.
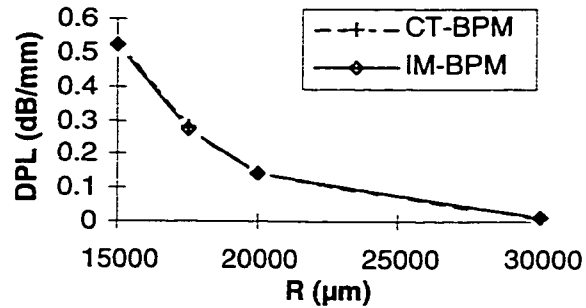
Figure 2.4: Differential power loss vs. bend radius for a singlemode fibre as calculated by the CT and IM BPMs.

There are two sources of loss, namely, transition loss and bending loss. The transition loss (TL) is due to the change in the mode shape at the junction of straight and bent sections and the bending loss is manifested as a constant differential power loss (DPL). Figure 2.4 shows the DPL as calculated by both methods for varying radius of curvature. The two methods agree for this case, due to the large R's.

2.4.2 Rectangular channel guides

In this section, simulations of singlemoded rectangular waveguides useful for the construction of integrated optic devices are presented. These guides typically have smaller cross-sections and higher index differences than fibres to increase integration density and thereby decrease overall device size. It is therefore important to accurately calculate the minimum acceptable bend radius. The particular case chosen here is a square guide 2.5 μm on a side and having refractive indices 1.56 and 1.50 for the core and cladding areas respectively. This waveguide is singlemoded for the simulation wavelength, $\lambda = 1.55\,\mu m$.
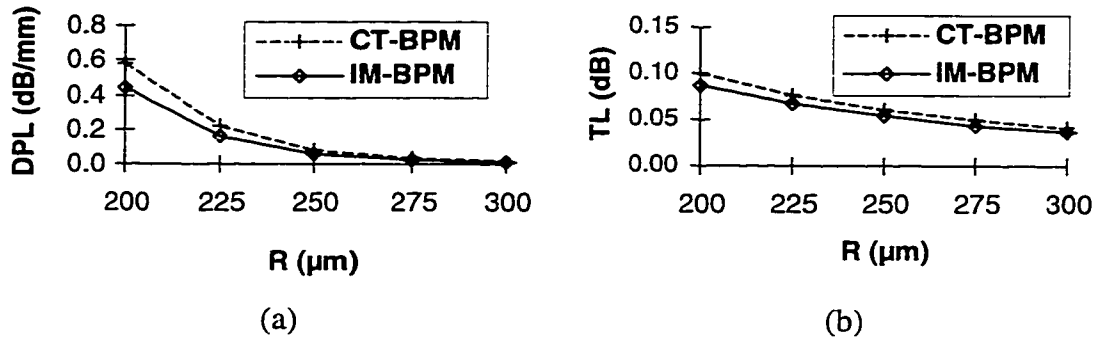
Figure 2.5: (a) differential power loss and (b) transition loss vs. bend radius for a singlemode waveguide calculated by both the CT and IM BPMs.

Figure 2.5 shows the results of simulations giving the two sources of loss as a function of bend radius. As expected, the difference between the two methods becomes more pronounced as R decreases. In addition, the results of the CT-BPM show higher losses than the results of the IM-BPM. Significant differences between the results of these two approaches can be expected for $R \ll 1\,mm$.

2.5. Discussion

A novel approach for the simulation of bent waveguides using the BPM has been presented. The method entails a coordinate transform to simplify the formulation of a three dimensional wide-angle BPM in cylindrical coordinates. The calculations have been implemented on a path-based grid, which can follow arbitrarily bent waveguides. This new method, which includes the complete diffraction term in the out of bend-plane direction, predicts higher bending and transition losses than the earlier IM-BPM, especially for small, singlemode waveguides, which may also have small radii of curvature. A verification of these calculations by experiment is difficult because other sources of loss will tend to limit the precision with which the experiment can be performed. Examples of the types of losses which would be difficult to separate form the contributions of the DPL and the TL are material losses, side-wall roughness, coupling

18

losses, etc. To the best of the author's knowledge, there have been no reports of loss measurements on similar singlemode waveguides with such small bending radii.

3. Graded Effective Index Planar Polymer Waveguides

3.1. Introduction to Passive Waveguide Devices

Polymer waveguides are of current interest for low-cost optical interconnects between electronic processing chips in hybrid optoelectronic integrated circuits [27]. Most of the work to date has been in multimode (MM) step index structures which are easy to produce, have good coupling properties to sources and detectors, and whose loss and dispersion characteristics are adequate for wafer-scale applications. Some of the methods for fabricating polymer waveguides are selective curing (either photolithographically [28] or by laser writing [29]), similar selective exposure of photorefractive materials [30], and direct dispensing of UV-curable adhesives [31].

Another potential application for polymer waveguides is in guided wave optical buses in digital equipment such as computers or switches where the required transmission distance would be up to 0.5 meter. Terabit bus capacity could be achieved with 100 waveguides each carrying 10 Gb/s of information. One hundred waveguides on 250 μm centers would occupy a 2.5 cm or 1 inch strip, notwithstanding extra space required for connector housings, etc. Current waveguide losses of 0.2 dB/cm [32] result in an acceptable end-to-end loss of 10 dB but dispersion in step index waveguides may not be acceptable. For example, assuming an index of refraction n = 1.5 and a relative index difference between core and cladding, Δ = 1%, the worst-case dispersion-limited distance for a 10 Gb/s signal is 0.5 m [33] leaving no margin for other system rise-times. Lowering the bit rate and increasing the number of waveguides would only be a stopgap solution since, ultimately, higher capacities would be required.

3.2. Graded Effective Index Guides

Modal dispersion can be eliminated completely by using singlemode (SM) waveguides and conceivably, 0.5 m long, low-loss SM waveguides could be fabricated. Another option, used in fibre optics before SM fibres became commonplace, is to use graded-index (GRIN) MM waveguides. With the proper profile, such waveguides can have modal dispersion nearly 3 orders of magnitude smaller than that of step-index MM waveguides [34]. There have been reports of GRIN planar waveguides [35,36] and some analysis has appeared in the literature [37,38]. There have also been reports of polymer waveguides with the index graded in the out-of-plane direction, for the purpose of replacing a cladding layer [39].

This section presents novel planar graded effective index waveguides that are easy to fabricate and have properties similar to quadratic index waveguides. They are essentially polymer slab waveguides with parabolic surfaces that lead to near-quadratic effective indices of the slab mode. In Section 3.2.1, the fabrication of the waveguides and measurements of the waveguide loss are described. Images are shown of side-scatter from propagating light along with simulation results that are in excellent agreement. A simple analysis is given in Section 3.2.2 to explain the origin of the graded index behaviour and some details of the computer simulations are also explained. Concluding remarks and a summary of the work are given in Section 3.2.3.

3.2.1 Fabrication and measurement

The waveguides were made by direct dispensing from a pressurized syringe under computer control [31] of a UV-cured polymer optical adhesive (NOA 81 [40]) with index of refraction $n_p = 1.56$. Of the many different adhesives available, this one was chosen because its very low viscosity leads to a low height:width ratio of the waveguide. The substrate was a silicon wafer with a 5 µm surface layer of silica grown by chemical

vapour deposition. This layer acts as the lower cladding of the waveguide and has index

of refraction n_s = 1.45. From experience with dispensed optical elements, it has been

found that the most consistent results are obtained when the dispensed liquid is allowed

to come to equilibrium before curing. Then each polymer has a unique contact angle

with the glass surface, which is determined by the liquid/air and liquid/glass surface

tensions. Due to the minimization of surface energy, the surface profile is a circular arc,

which for small height:width ratios of the polymer is very close to parabolic. Figure 3.1

shows the cross-section of one of the waveguides along with a parabolic least squares fit.

The height:width ratio is approximately 1:100. If necessary, an upper cladding can be

dispensed over the core.
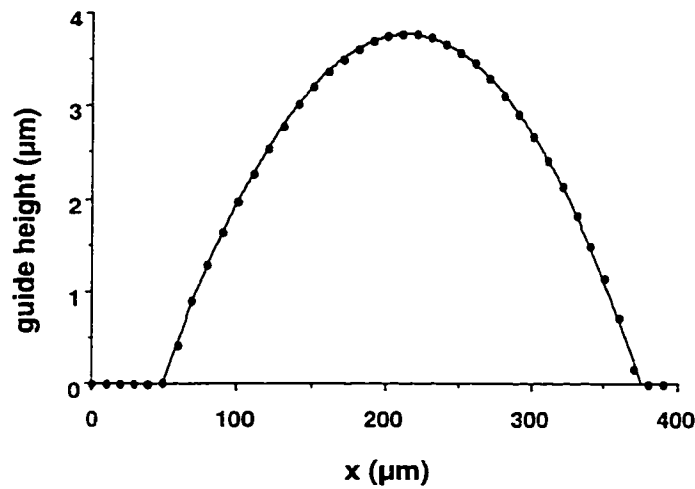
Figure 3.1: Typical cross-section of a parabolic waveguide. The dots are points measured
with a profilometer and the solid line is a parabolic fit to the data.

Propagation experiments were carried out by butt-coupling a singlemode fibre

carrying 672 nm light to the input facet of the waveguide as shown in Figure 3.2. By

measuring the intensity of the transmitted light as a function of guide length, waveguide

losses were inferred. Figure 3.3 shows linear fits to the relative power measured in dB of

several waveguides. The losses ranged from 0.69 dB/cm to 0.48 dB/cm. An upper

cladding of lower index polymer could be applied which was observed to reduce

scattering losses; however, this was not done for the waveguides reported here since the

side-scattered light became too dim to observe. Such an upper cladding would be expected to alter the details of the propagation characteristics reported here, though not in a fundamental way.
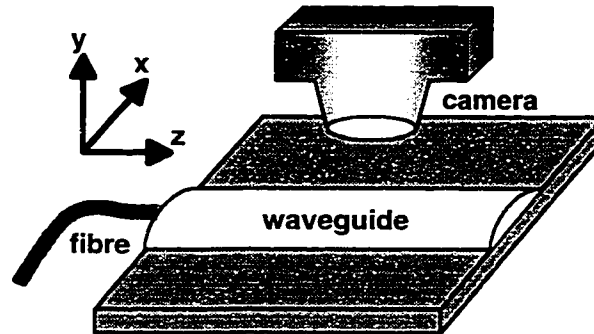
Figure 3.2: The experimental setup. The input fibre carries 672 nm light and is held in a 3-axis positioner. The waveguide is on a SiO_2 coated silicon substrate. The camera detects the light scattered out of the top of the guide.
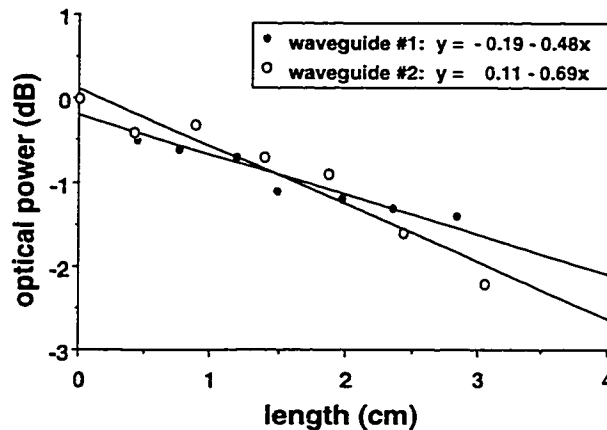
Figure 3.3: Cut-back measurement of transmitted light from dispensed graded effective index waveguide, and determination of the propagation losses for two sample waveguides giving .48dB/cm and .69dB/cm respectively.

Different launching conditions were set up by changing the lateral position of the fibre at the input face and the propagation paths of the light in the waveguide were recorded by capturing images of the side-scattered light with an electronic camera. The graded index behaviour of these waveguides is best illustrated when the light is launched off-axis. Figure 3.4(a) shows a typical side-scatter pattern near the input when the light is launched approximately 110 μm off-axis into a waveguide with the profile shown in

23

Figure 3.1. The corresponding computer simulation results, described in the next section, are shown in Figure 3.4(b). The input beam splits into several oscillating beams each with its own period and each beam propagates several millimeters without showing appreciable spreading in size. Figure 3.5(a), another side-scatter pattern approximately 2 mm down-stream, shows the oscillating beams still confined as before. The corresponding computer simulation results, again in excellent agreement, are shown in Figure 3.5(b).
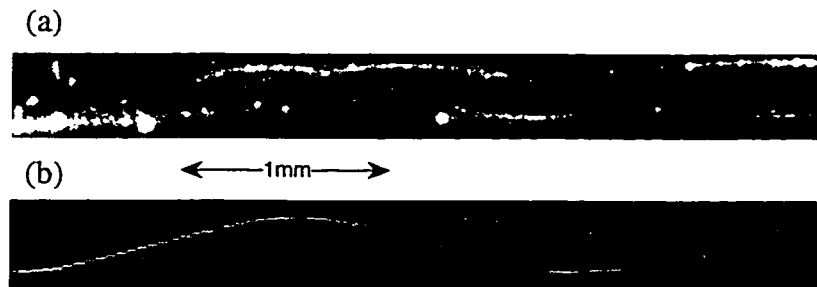
Figure 3.4: (a) Picture taken of experiment starting from the launch, and (b) beam propagation simulation on the same scale showing the dependence of the oscillation length on the mode number. The fibre is off-axis by approximately 110 μm.
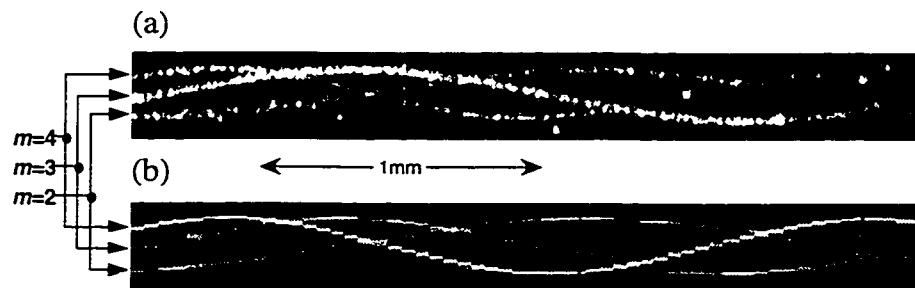
Figure 3.5: (a) Picture taken of experiment approximately 2 mm from launch, and (b) beam propagation program output shown on the same scale. The three modes with measurable lateral oscillation period are indicated on both images. The fibre is off-axis by approximately 80 μm in this case.

As shown in the next section, each of these beamlets corresponds to a different vertical mode of the asymmetric polymer slab, and each has its own laterally graded effective index. Table 3.1 shows the measured and predicted periods for each mode, with the larger mode numbers having the smaller periods. The periods of the first and second modes (m = 0 and 1 respectively) can not be measured using the image of Figure 3.5 for

24

two reasons: (1) they are too long for an appreciable number of oscillations to be seen in the limited field of view of the camera; and (2) the size of the mode in the lateral direction throughout most of the guide is large making the average power density too low to be picked out among the brighter high order modes.

Mode Number, m	Experiment (mm) ±5%	Model (mm)
launch conditions shown in Figure 3.4		
0	-	10.
1	-	5.0
2	3.3	3.6
3	2.7	2.7
4	2.2	2.3
Launch conditions shown in Figure 3.5		
0	8.3	8.1
1	3.6	4.0
2	2.4	2.7

Table 3.1: The comparison of oscillation lengths for different modes from the experiment and model for the two different launch conditions corresponding to Figure 3.4 and Figure 3.5.

3.2.2 Theory and simulation

In this section, we explain the theory behind the simulation results presented above. Polarization effects were ignored and the electric field $E(x,y,z)$ in the central region of the dispensed polymer-on-glass waveguide was assumed to satisfy the scalar wave equation

$$\frac{\partial^2 E}{\partial x^2} + \frac{\partial^2 E}{\partial y^2} + \frac{\partial^2 E}{\partial z^2} + n^2(x,y)k_0^2 E(x,y,z) = 0. \tag{3.1}$$

Here, $k_0 = 2\pi/\lambda$ (λ is the wavelength of the light in vacuum) and $n(x,y)$ is the refractive index. The polymer core has width w and slowly-varying thickness $h(x)$ given by

$$h(x) = h(0)\left(1 - 4x^2/w^2\right) \tag{3.2}$$

while $n(x,y)$ is given by

25

$$n(x,y) = \begin{cases} n_s & \text{for} & y < 0 \\ n_p & \text{for} & 0 < y < h. \\ 1 & \text{for} & y > h \end{cases} \qquad (3.3)$$

Here n_s and n_p are the indices of the substrate and polymer respectively. At each lateral position x, the guided field may be expanded in terms of a set of M local guided asymmetric slab waveguide modes as

$$E(x,y,z) = \sum_m^M E_m(x,z) S_m(y) \exp(-j\beta_m z) \qquad (3.4)$$

where $S_m(y)$ are orthogonal functions of the form [41]

$$S_m(y) = N_m \begin{cases} \exp(\alpha_m y) & \text{for} & y < 0 \\ \cos(K_m y - \varphi_m) & \text{for} & 0 < y < h \\ \exp(-\gamma_m(y-h)) & \text{for} & y > h \end{cases} \qquad (3.5)$$

K_m, α_m, φ_m, and γ_m are propagation constants chosen to satisfy the boundary conditions at the interfaces $y = 0$ and $y = h(x)$, and N_m is a normalization constant. Therefore $S_m(y)$ depends on the lateral coordinate, x, explicitly through $h(x)$ and implicitly through the propagation constants. Substituting (3.4) into the wave equation and using the orthogonality of the slab modes, an equation for each $E_m(x,z)$ is obtained:

$$\frac{\partial^2 E_m}{\partial x^2} + \frac{\partial^2 E_m}{\partial z^2} + \left[n_p^2 - \frac{K_m^2(x)}{k_o^2} \right] k_o^2 E_m(x,z) + \text{extra terms} = 0 \qquad (3.6)$$

The extra terms are quite complicated, containing first and second derivatives of $h(x)$ and the propagation constants with respect to x, as well as integrals over y of different combinations of the orthogonal functions and their derivatives. Fortunately, these terms will be small, since the core thickness varies slowly in x, and are neglected here. If included, these terms would cause coupling between the various slab modes. The quantity in square brackets in (3.6)

$$n_m^2(x) = [n_p^2 - K_m^2(x)/k_0^2] \qquad (3.7)$$

26

is the graded effective index of the mth slab mode. Since each slab mode has a different $K_m(x)$, each will see a different graded effective index leading to different periods of oscillation about the waveguide axis.
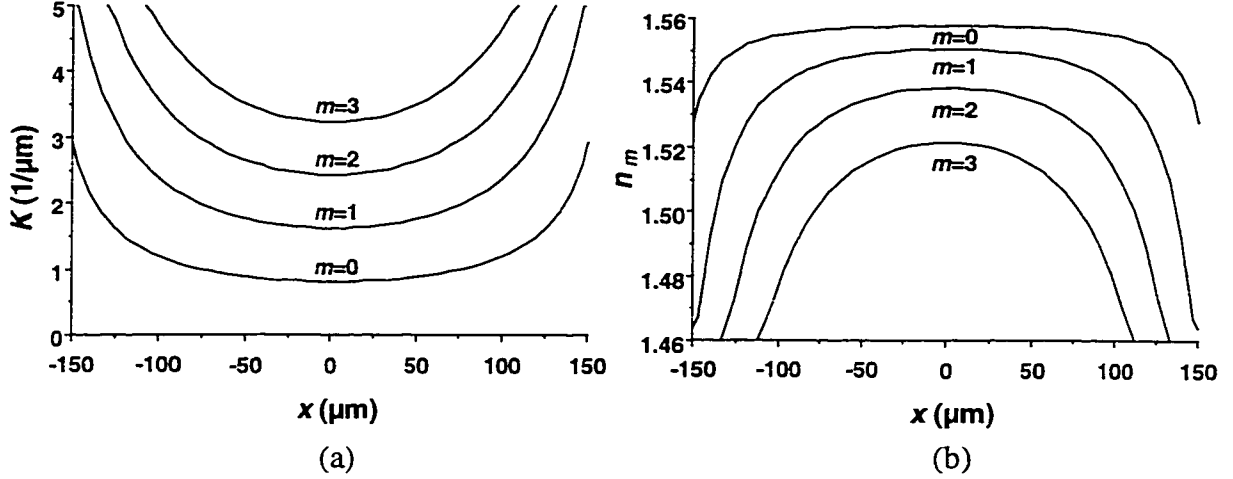
Figure 3.6: (a) The solution for $K_m(x)$, defining the effective index profile, as a function of x in a parabolic height waveguide having height 3.6 μm and width 340 μm for a wavelength of 672 nm. The solution is shown for several modes (m=0 through 3). (b) The graded effective index $n_m(x)$ for each mode determined from $K_m(x)$ Note that each mode sees a different effective index profile.

Equation (3.6) was solved by a scalar beam propagation code originally written to simulate multimode polymer waveguides [42] and modified to accommodate an index graded in x. First, the functions $K_m(x)$ and $n_m(x)$ were found by numerically solving the asymmetric slab waveguide equations with the measured parabolic profile given by

$$h(x) = (3.60\mu m)[1 - 4(x/340\mu m)^2]$$ (3.8)

and a wavelength of 672 nm. Plots of $K_m(x)$ and $n_m(x)$ as functions of x and mode number, m, are shown in Figure 3.6. A gaussian input of the form

$$E(x, y, 0) = E_o \exp\left[-\frac{(x-d_x)^2 + (y-d_y)^2}{2\sigma^2}\right]$$ (3.9)

was assumed. The launched light was then split up into vertical modes using each field pattern, $E_m(x,0)$, as determined numerically from the overlap integral of the input and the mth slab mode about $x = d_x$ which was picked to correspond to the experimental

27

launching condition. The beam size, σ, was set to 3 μm to correspond to the output of the singlemode fibre delivering the light to the waveguide. The only unknown parameter is the vertical offset d_y which could not be determined and which affects the relative amplitudes of the modes.

(a)

(b)
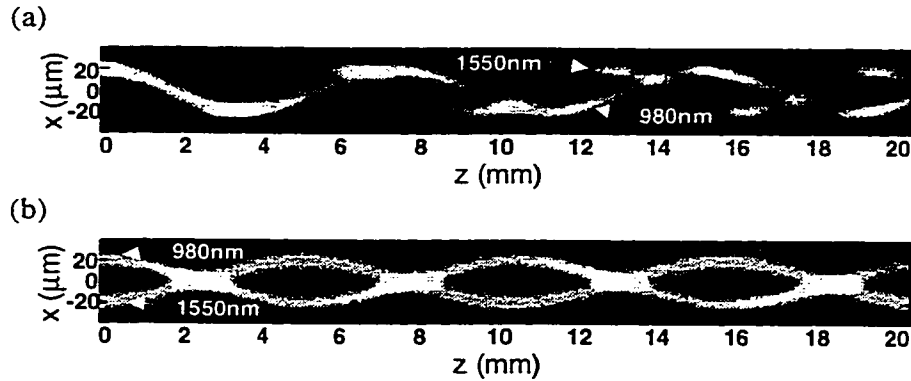
Figure 3.7: (a) Simulation results for the demultiplexing of multiplexed 980 nm and 1550 nm beams. The modeled waveguide is singlemoded in the vertical direction having height 2.75 μm and width 260 μm. (b) Similar simulation showing the same graded effective index effect for the two wavelengths. The two wavelengths are launched on opposite sides of the axis. This waveguide has height 2.18 μm and width 400 μm.

The graded effective index will also be a function of the wavelength λ. Figure 3.7(a) shows the simulation results of two multiplexed beams of light at 980 nm and 1550 nm launched off-axis into a 2.75 μm high by 260 μm wide waveguide which supports only one slab mode at both wavelengths. This was achieved by assuming a polymer substrate with an index slightly lower than that of the core. The material dispersion was included by using the following values (obtained from the supplier): 1.546 and 1.541 at 980 and 1550 nm, respectively, for the core polymer and 1.529 and 1.525 at 980 and 1550 nm, respectively, for the substrate polymer. After a distance of 19 mm, the two signals are separated and could be channeled in different directions by pickup waveguides, possibly laser-written in polymer. This calculation demonstrates that such waveguides are an alternative to step-index multimode interference waveguides that have been proposed for coarse wavelength division multi/demultiplexing devices [43].

28

It should be noted that normal material dispersion, that is, $dn/d\lambda < 0$, lessens the wavelength dependence of the graded effective index effect described above. Figure 3.7(b) shows a similar calculation in a waveguide 2.18 μm high by 400 μm wide, but with the two wavelengths launched on opposite sides of center to make the result more visible. The two beams now have approximately the same period. This would be advantageous in situations were the two wavelengths should follow the same paths in the waveguide. For example, in an Er-doped waveguide amplifier carrying 980 nm pump light and 1550 nm signal light, the performance would be degraded by misalignment of the input fibre if the two beams were to spatially separate in the waveguide.

Further work has been performed using these waveguides which were dispensed onto a bulk Erbium/Ytterbium co-doped glass [44]. The result was a waveguide that exhibited the properties of optical amplification. The waveguide structure was not optimal but was able to reach the "break-even" point, i.e., the signal enhancement was enough to overcome the propagation losses in the waveguide.

Future work is planned to fabricate graded effective index waveguides and step index waveguides with lengths of one meter. Using femtosecond laser pulses, the aim is to experimentally measure dispersion in the two structures. This experiment should verify the hypothesis that the graded effective index structure can be used to lessen the dispersion penalty on this length scale.

3.2.3 Discussion

We have demonstrated graded index behaviour in thin dispensed polymer waveguides. The theoretical analysis of these waveguides, which has no free parameters, is in excellent agreement with the measured properties indicating that this phenomenon is well understood. The waveguides demonstrated in this paper have several modes, each of which sees a different graded effective index. By applying another polymer with

29

index slightly lower than the core as an upper cladding, the waveguides could be made to have only a single vertical mode. Because these waveguides are easy to fabricate and show low loss (which should be reduced even further with an upper cladding), they are candidates for ultrahigh speed board-scale interconnects where dispersion will be a factor. Also, because they are wavelength-dependent, they may be used as coarse WDM devices.

4. Polymer Electrooptic Modulator/Switch

The device that will be discussed in this chapter is a polymer electrooptic modulator/switch (POEMS). It is configured as a 2X2 optical switch; however, if only one input is selected, it can be used as a modulator with a complementary output. Versions of the device have been designed to work at wavelengths of 1320 nm and 1550 nm. The target performance is a bandwidth suitable to transmit 10 Gb/s and an insertion loss of no more than 6 dB. This device has many unique features, which will be discussed in turn.

A polymeric 2X2 EO switch has been reported by Hwang et al. [45]; however, it lacks many of the important features of the POEMS device. This previous device was created using asymmetric Y junctions to achieve the necessary coupling at the input and output of the device. These junctions require branching waveguides that intersect at very small angles (~0.2°), which can cause problems in fabrication such as fill-in between the waveguides. The POEMS device employs multimode interference (MMI) couplers to achieve the needed coupling. These couplers have the advantages of being easily designed [46], having reasonable fabrication tolerances [47], and being rectangular in shape they have fewer problems with fill-in during fabrication as do asymmetric Y junctions.

Two additional important features of the POEMS device not present in the Hwang device involve the electrical drive. The POEMS device uses coplanar electrodes to both pole and drive the device, resulting in the two arms of the interferometer being driven in a push-pull fashion by a single applied signal. Also, the electrical signal on the coplanar electrodes is velocity-matched to the optical signal, producing a travelling wave device.

The use of coplanar electrodes has also been reported [48-51]. All of these papers, except [51], report on the measurement of the EO coefficients of polymer films in

31

which there is no waveguiding action, i.e. the direction of light propagation is normal to the surface of the substrate and the coplanar electrodes. Reference [51] describes a waveguide device having coplanar electrodes in the plane of the light propagation. The device could be poled to produce a push-pull interferometer but the electrical signal could not be velocity-matched to the optical signal. This device was a simple modulator, having one input and one output, and was limited to 4 MHz bandwidth.

4.1. Introduction to Electrooptic Polymers

Before the advent of electrooptic (EO) polymers, the most common materials used in the study of the linear EO effect were anisotropic crystals, in particular, lithium niobate because of its large EO coefficient. The restriction to anisotropic materials is problematic for most polymers, as the material is a group of randomly oriented chains of molecules. The random nature of the structure on a molecular scale produces an isotropic material for optical considerations. The solution is to introduce a highly EO component, such as an organic dye molecule, into the polymer. These molecules must then be aligned to produce the needed asymmetry.

The dye molecules are natural dipoles, which can be aligned using an electric field. If the polymer dye combination is heated, the polymer will go through a glass transition, so that the dye molecules can move more easily. An electric field is then applied to the structure, and the temperature is lowered, effectively freezing the dye molecules in their ordered orientation. This process is known as poling the polymer [52]. The problem in this process is that at any finite temperature, the random motion of the molecules, although restricted, will tend to destroy the orientation of the dye molecules, causing decay in the performance of the device [53].

32
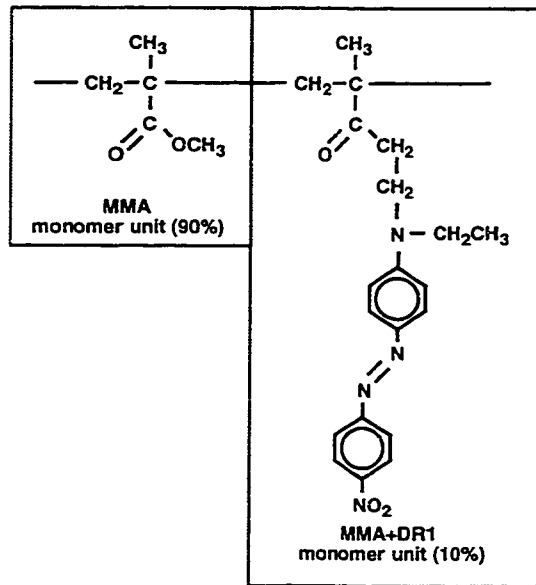
Figure 4.1: Chemical composition of DR1-PMMA EO polymer

The EO polymer chosen for this research has the dye molecule chemically bonded to a monomer unit as a side chain and is shown diagrammatically in Figure 4.1 [54]. The polymer is poly(methylmethacrylate) (PMMA) with 10% of the monomer blocks having a side chain dye molecule called Disperse Red 1 (DR1) and will be referred to as DR1-PMMA.

An improvement in the side chain polymers is possible by modifying the polymer to allow cross-linking. This gives the polymer chains the ability to chemically bond to each other, further limiting the mobility of any side chains. Cross-linked polymers are more durable, more resistant to chemical attack and have higher glass transition temperatures than their non-cross-linked counterparts. Cross-linked EO polymers show promise for the long-term stability of device performance [55,56].

EO polymers have several advantages as materials for devices over crystalline materials. Since the polymer can be dissolved, it can be cast into almost any shape. Also, EO polymers have an additional degree of freedom; the poling field defines the direction of the optic axis. Unique devices having twisted optic axes have been demonstrated [57], a possibility which did not exist before EO polymers. EO polymers

33

also promise extremely fast devices, such as a recently reported intensity modulator with a bandwidth of 110 GHz [58].

4.2. Phase Modulation and the Mach-Zehnder Interferometer

EO polymers exhibit the linear electrooptic or Pockels effect, which is a linear change in the index of refraction of a material as a function of applied electric field. EO polymers are uniaxial anisotropic materials such that they exhibit two values of refractive index depending on the polarization of light with respect to a direction in the material called the optic axis. The two indices of refraction, are given by

$$n_o(E) = n_o + \tfrac{1}{2}n_o^3 r_{13} E \qquad (4.1a)$$

and

$$n_e(E) = n_e + \tfrac{1}{2}n_e^3 r_{33} E , \qquad (4.1b)$$

where n_o is the base ordinary refractive index (for light polarized perpendicular to the optic axis), n_e is the base extraordinary refractive index (for light polarized along to the optic axis), the r_{ij}'s are the non-zero elements of the tensor that describes the EO effect and E is the applied electric field (assumed to be applied along the optic axis) [59]. The material properties of the EO polymer result in r_{33} being three times larger than r_{13} [54]; therefore the device will be constructed to exploit the effect described by equation (4.1b). This equation corresponds to the refractive index for light polarized along the optic axis. The direction of the optic axis in EO polymers is defined by the direction of the poling field, thus, all of the electric fields (optical, poling and modulation) point along the optic axis in this case. The magnitude of the EO coefficients of the polymer is proportional to the applied poling field. In the case of DR1-PMMA the relevant coefficient can be determined from the following relation which was supplied by the manufacturer:

$$r_{33} = 0.050 E_{poling} , \qquad (4.2)$$

where r_{33} is given in units of pm/V if E_{poling} is the poling field in units of $V/\mu m$.

The usual change of index in EO polymer is very small, making it necessary to construct devices that are sensitive to the change in phase of light propagating through the polymer. An interferometer is the device of choice for this purpose. Of all the varieties of these, the Mach-Zehnder interferometer, shown schematically in Figure 4.2, is the most versatile for implementation in waveguide devices.
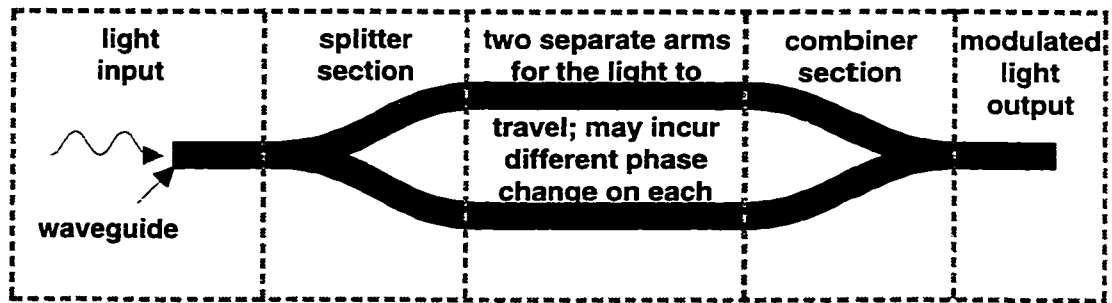
Figure 4.2: Schematic of a waveguide Mach-Zehnder interferometer.

Mach-Zehnder interferometers work by splitting the light from a single source, propagating the light along two separate paths and then interfering the light from these two paths to produce a modulated output. The modulation depends on the light from the two arms incurring different phase changes, in this case provided by a change in the index of refraction through the EO effect.

4.3. Optical Properties of the Materials

The optics of the POEMS device are constructed in a unique combination of materials, namely, EO polymer and fused silica. Traditionally, EO polymer devices have been constructed in a combination of passive and EO polymers to produce the optical waveguide structure. This approach allows a great deal of flexibility in the design of a device, such as vertically stacking waveguides to produce multilevel devices [60]. This flexibility comes at the expense of fabrication difficulties. Photolithography followed by reactive ion etching (RIE) is often used to produce EO polymer waveguides [61]. Since the photoresist used in photolithography is a polymer, the RIE will affect both the resist

35

layer and the EO polymer layer. The choice of solvents used to remove the photoresist and to dissolve other polymers to be spin cast into cladding layers can also be problematic.

There are many reasons for choosing fused silica as the substrate and cladding material. It is highly transparent in the wavelength region of interest and has an index of refraction less than that of the EO polymer. It provides structural strength and is easily patterned using RIE. Fused silica has been proven to withstand fields as large as 370 V/μm during in plane poling of EO polymer, [62]. In addition, as will be discussed in Section 4.6, it has electrical characteristics that make velocity-matching simple using coplanar electrodes.

h=(1.5±0.3)μm
w=(2.0±0.2)μm

☐ air
☐ fused silica
▨ EO polymer
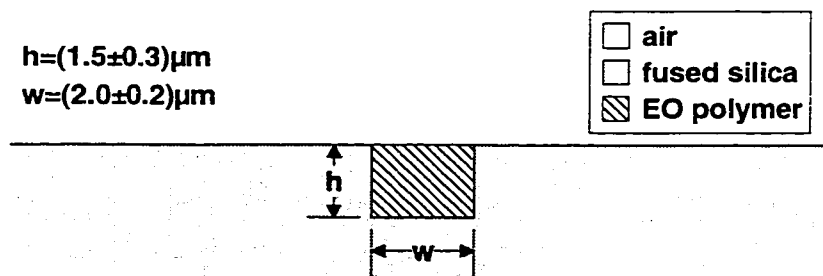
Figure 4.3: Cross-sectional view of the singlemode EO polymer waveguides. The guide is singlemoded throughout the range of height and width values specified by the tolerances at both λ=1.55 μm and 1.32 μm.

The geometry of the singlemode waveguides used throughout the device is shown in Figure 4.3. The dimensions of the waveguides have been assigned tolerances to allow for fabrication errors while keeping the guides singlemoded for both wavelengths of interest. Table 4.1 summarizes the refractive index values for each material as well as the range of effective propagation index defined by the extremes of the waveguide dimensions.

36

Wavelength (nm)	n, fused silica	n, DR1-PMMA	n_{eff}
1320	1.447	1.555	1.488-1.513
1550	1.444	1.550	1.469-1.497

Table 4.1: Material indices for both design wavelengths (the index given for the polymer is after poling). The range of effective index, n_{eff}, is determined from the extremes given the tolerances provided on the dimensions of the waveguides for light polarized with its E-field horizontal.

4.4. Multimode Interference Waveguide Couplers

The interferometer shown in Figure 4.2 is constructed using waveguide Y-branches, and therefore has a single input and a single useable output. There are actually two outputs, the second of which is radiated or unguided light. If, instead of Y-branches, multimode interference (MMI) couplers are used, one can construct a 2X2 optical switch using the same two-arm interferometer. Figure 4.4 shows a schematic of the POEMS device employing MMI couplers for both the input and output sections.
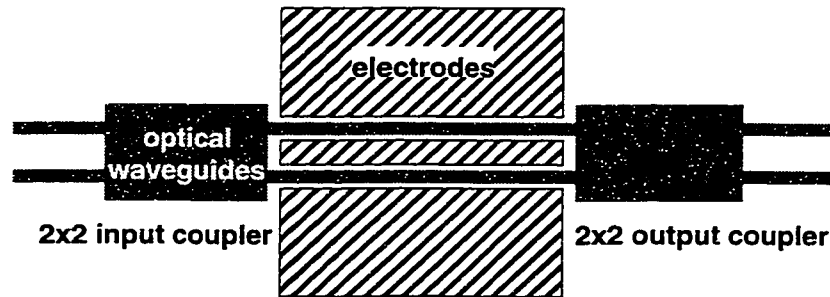
Figure 4.4: Schematic top view of the POEMS device. MMI couplers are used at the input and output to produce the 2X2 optical switch. The electrodes shown are used to apply both the driving and poling fields. The driving signal is applied to the electrodes using special coplanar probes that can be mounted above the substrate (see Section 4.11).

MMI couplers, as their name suggests, rely on the interference of multiple modes to produce images of an input field pattern. For example, one input waveguide may image to several output guides or vice versa. The implementation of these couplers in planar waveguides has a similar cross-section to the singlemode waveguide shown in Figure 4.3. The height, h, remains the same, but the width, W, of the MMI coupler section will be much greater, allowing multiple modes to propagate in that direction.

37

MMI couplers are sensitive to the phase of the light in the input guides such that an input can be imaged to one, both or the other of the two output guides of the 2x2 couplers (Figure 4.4) depending on the phase of the light exiting the two arms of the interferometer.

Design of these couplers makes use of an imaging length defined as [46]

$$L_\pi = \frac{4n_r W_e^2}{3\lambda_o}$$ (4.3)

where n_r is the effective index of the slab waveguide in the vertical direction, λ_o is the wavelength of the light, and W_e is the effective width of the MMI section given by

$$W_e = W + \frac{\lambda_o}{\pi\sqrt{n_r^2 - n_c^2}}$$ (4.4)

where W is the width of the MMI section and n_c is the index of the cladding material on either side.

Although the inputs of the MMI coupler can be placed at arbitrary positions along its edge, it is useful to restrict the positions to even intervals in W_e. This produces what is termed "restricted interference" and has the effect of reducing the needed coupler length by a factor of 3 [46]. For a 2X2 coupler, having inputs and outputs at $\pm W_e / 6$, the total coupler length is given by

$$L_{MMI} = \tfrac{1}{2} L_\pi.$$ (4.5)

To design the couplers, it is convenient to start by choosing a width for the MMI section. This section must support a sufficient number of modes to produce good images and keep the input and output guides separated by a reasonable distance. The rest of the parameters can then be calculated. Table 4.2 summarizes the results for a 2X2 MMI coupler having guide height, $h = 1.5\mu m$, and width, $W = 30\mu m$ composed of unpoled EO polymer having refractive index $n = 1.545$ and 1.539 at wavelengths of 1320 nm and 1550 nm respectively.

Wavelength (nm)	n_r	W_e (μm)	L_{MMI} (μm)
1320	1.513	31.0	732
1550	1.499	31.2	629

Table 4.2: Design results for the 2X2 MMI coupler sections.

These results were fine-tuned using the BPM to give, in each case, a maximum excess coupler loss of 1.5 dB and minimum contrast between output guides of 20 dB. Figure 4.5 shows the results of a BPM simulation to determine the excess loss of a MMI coupler when the same tolerances are used for the width of this section as were specified for the singlemode waveguide sections.
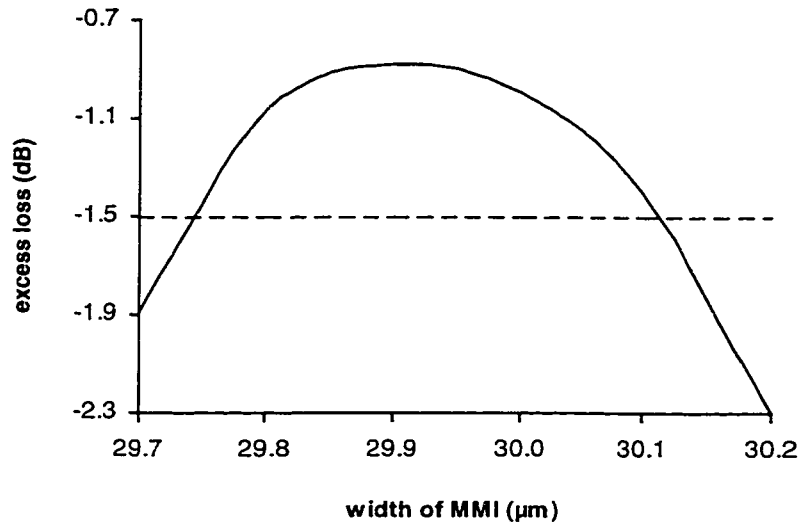
Figure 4.5: Calculation of the excess loss of an MMI coupler vs. the width of the MMI section using the BPM. The MMI coupler was 630 μm long and the simulation wavelength was 1550 nm. The tolerances assigned to the fabrication of the singlemode waveguides (± 0.2 μm) result in a maximum excess loss of 1.5 dB when applied to the width of the MMI sections.

4.5. Minimum Waveguide Bend Radius

The waveguides in the POEMS device must have a variable separation throughout different sections of the device. To achieve this, bends of some minimum radius of curvature can be used. These bends are s-shaped sections which are realized using rotated sine curves such that there is zero curvature at both ends where they match to

straight waveguides. The minimum acceptable radius of curvature for these bends was estimated using constant radius bends in the CT-BPM described in Chapter 2.
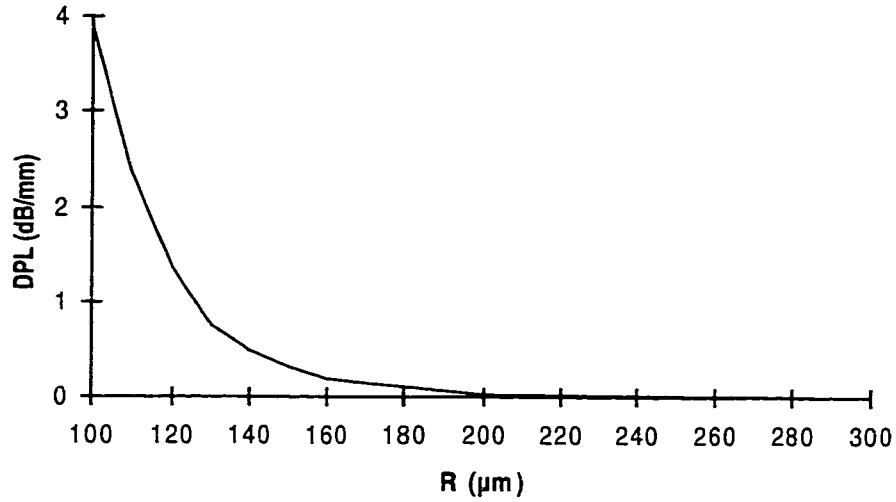
Figure 4.6: Results of BPM simulations of the singlemode waveguides used in the POEMS device showing the DPL vs. bend radius for constant radius bends.

All of the bends used in the design of the POEMS devices have minimum radii of curvature greater than 400 µm which ensures that bending losses will be insignificant compared to losses due to material absorption and side-wall roughness in the waveguides.

4.6. Microwave Coplanar Waveguides

There are many choices of transmission lines that can be fabricated on planar substrates to carry high-speed electrical signals, some of which are shown in Figure 4.7. Of these, slotline is rarely used for EO devices as it is difficult to couple to and is usually used for high power applications.
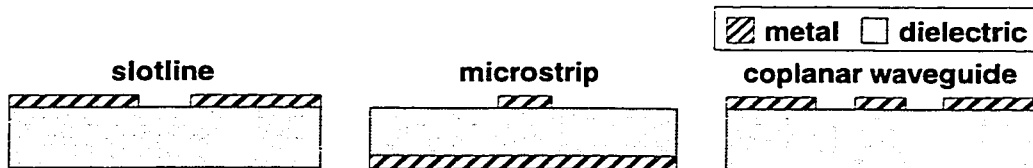
Figure 4.7: Cross-sectional view of three different planar transmission lines.

40

Microstrip is the most commonly used transmission line for EO polymer devices. When utilized in a Mach-Zehnder interferometer, the optical waveguides are placed directly underneath the top electrodes, such that the maximum field is applied to the EO polymer. The remainder of the dielectric is composed of a passive polymer; however, typical polymers have high loss in the near infrared due to vibrational overtones of C-H bonds. Replacing the hydrogen in the cladding polymer with deuterium has been shown to lower the loss in the optical waveguides [60].

To achieve the minimum drive voltage, both arms of the interferometer must be driven by electrical signals, creating two choices. In the first case, different signals are used, where one may simply be the inverse of the other to achieve the opposite phase shift on each arm. If applied using microstrip, the electrodes must be separated by enough distance to reduce the coupling of fields from one line to the other. The structure of microstrip results in large fringing fields that make this difficult. This approach has the advantage that the EO polymer in both arms of the interferometer is poled in the same direction. In this configuration, the polymer can be poled by corona [63] or liquid contact [64] poling before the waveguides are formed. Both of these methods have been shown to produce very high poling fields with relatively little damage to the polymer film as compared to electrode poling using microstrip.

The second choice to drive the two arms of the interferometer is to use the same signal on both arms. This requires that the EO polymer in the two arms be poled in opposite directions to achieve the opposite phase shift on each arm. A technique called pulse-poling [65] can be used to achieve the correct poling directions while avoiding the breakdown of the air above the electrodes while the large poling fields are in place. The two electrodes used to pole the polymer can be designed to be 100Ω transmission lines which can be connected in parallel to maintain a 50Ω overall impedance [66].

Several problems exist in the use of microstrip electrodes for EO polymer Mach-Zehnder interferometers: (1) Most of the field surrounding the microstrip transmission line is concentrated in the dielectric resulting in a high effective index for the propagating electric field. (2) In order to velocity match the electrical and optical signals, the dielectric material must have very low dispersion from the electrical to the optical frequency range. This requirement essentially restricts the cladding material for the EO polymer to other polymer materials. 3. Electrode poling is the simplest way to pole the EO polymer; however, damage to the surrounding polymer effectively restricts the magnitude of poling field which can be applied. 4. The characteristic impedance of the microstrip transmission line is strongly affected by the thickness of the polymer cladding layer which can be difficult to control precisely. 5. The need to drive both arms of the interferometer creates added complexity in the design and fabrication of the electrode layout.
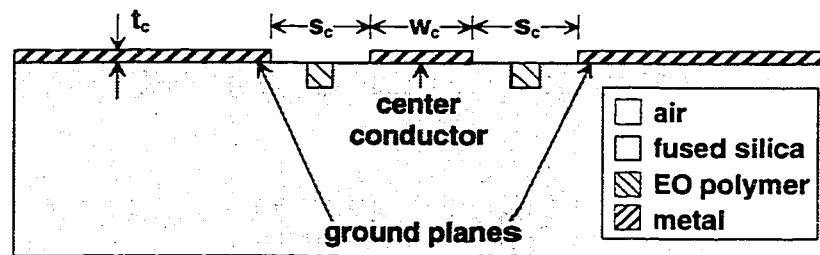
Figure 4.8: Cross-sectional view of the POEMS device. The critical dimensions of the metal electrodes are shown. They define the propagation characteristics of the coplanar waveguide transmission line.

The POEMS device employs coplanar waveguide (CPW) transmission lines as shown in Figure 4.8. These electrodes are used both to pole the EO polymer and to apply the driving signal. When poling the device, the poling potential is applied to one ground plane while the other is maintained at ground. The poling field is therefore applied in the same direction to both of the optical waveguides. During poling, the electrodes are temporarily covered over with a silicone dielectric fluid that is removed after the poling process. When driving the device, the signal is applied to the center conductor while

both of the ground planes are held at ground. In this way, the driving field is applied to each of the optical guides in the opposite direction causing a push-pull effect in the interferometer. This design is very simple in comparison to the implementation of a push-pull device using microstrip electrodes.

Another advantage of the CPWs is that approximately half of the electric field is in the air above the metal, which results in a reduced effective index seen by the electrical drive signal. This gives some flexibility to the choice of cladding materials, allowing a higher material dispersion from the electrical to the optical frequency range. Fused silica was chosen because of its moderate material dispersion and its optical transparency in the near infrared.

An approximate calculation to show the suitability of fused silica can be done as follows. The relative electrical permittivity of fused silica in the GHz region is $\varepsilon_r = 3.82$. The effective permittivity, ε_{eff}, of a CPW is defined as the permittivity of a material, which, when used to replace the materials above and below the CPW, results in the transmission line having the same characteristics as the original line. It is maximum when the metal layer is of negligible thickness. It can be shown for this case that ε_{eff} is the average of the substrate permittivity and the permittivity of the air above the CPW [67], giving $\varepsilon_{eff} = 2.41$. The propagation of the electrical signal on the CPW is described by a quasi-TEM mode which has an effective index of propagation, $n_{eff} = \sqrt{\varepsilon_{eff}} = 1.55$. Thickening the metal layer will raise the proportion of the field in the air thereby lowering the effective index. The effective index of a singlemode optical waveguide constructed in fused silica with a core of EO polymer, as given in Table 4.1 lies between 1.47 and 1.51 for the wavelengths of interest. The effective index of the CPW is only slightly higher than the range of the optical effective index providing the possibility of simple velocity-matching through the choice of metal thickness used to construct the CPW transmission lines.

43

4.6.1 Determination of Transmission Line Characteristics

There are three important characteristics of the CPW transmission line that impact the performance of the POEMS device. They are the characteristic impedance, Z_c, the effective index, n_{eff}, and the frequency dependent loss. The process used to pattern the electrodes includes a wet-chemical etch of the metal layer. This results in a curved side-wall at each conductor edge, as shown in Figure 4.9, owing to the isotropic nature of the etching process. The important dimensions are the metal thickness, t_c, the gap size, s_c, and the width of the center conductor, w_c. Both w_c and s_c are determined by the distances to the bottom of the cusps defined by the etching process.
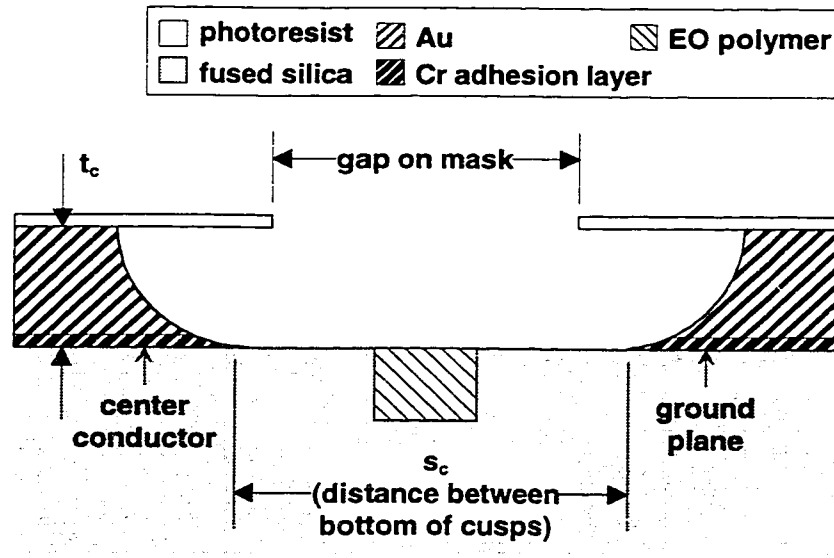
Figure 4.9: Cross-sectional view of the right hand side gap between the center conductor and the ground plane.

For the purposes of an EO modulator, it is advantageous to have a small gap between the conductors. If the gap size is comparable to the radius of the arc on the side-walls, it may not be valid to use expressions formulated for rectangular conductors, like the ones shown in Figure 4.8, to calculate the transmission line characteristics. Since CPW has a quasi-TEM mode, the impedance and effective permittivity can be determined solely from the capacitance per unit length, C/L, of the line [68]. The

capacitance per unit length can be determined for an arbitrary transmission line by evaluating the following integral

$$C/L = \oint dl \varepsilon \bar{E} \cdot \hat{n} \qquad (4.6)$$

where $\bar{E}$ is the electric field produced by a 1V potential applied to the line, ε is the local electrical permittivity, $\hat{n}$ is the outward pointing perpendicular unit vector to the path and dl traces out a closed path around the center conductor. The relative effective permittivity is then found by

$$\varepsilon_{eff} = \frac{(C/L)_{actual}}{(C/L)_{air}} \qquad (4.7)$$

where the numerator is the C/L with all of the materials in place and the denominator is the C/L with all materials replaced by vacuum ($\varepsilon_r = 1$). Then the characteristic impedance can be calculated using

$$Z_c = \frac{\sqrt{\varepsilon_{eff}}}{c(C/L)_{actual}}. \qquad (4.8)$$

To evaluate the integral (4.6), a finite element package called PDEase2 was used to determine the electrostatic field distribution surrounding the CPW. This approach, called the quasi-static approximation, is valid for electrical wavelengths much greater than the cross-section of the CPW. The quasi-static approximation has been reported in the literature applied to the problem of optimizing the electrodes of travelling wave electrooptic modulators [69]. By symmetry, only half of the structure needs to be calculated and the integral from one half can be doubled to get the total C/L. A rectangular integration path is used for simplicity such that the unit normals single out the contribution of E_x and E_y on the horizontal and vertical segments respectively. Figure 4.10 shows one such solution for the right hand side of a CPW.

The free parameter, which was varied for the design of the POEMS device, was the gap size, s_c. The other CPW dimensions are then fixed by the choice of the

45

transmission line characteristics, namely the characteristic impedance and the effective

index. The design requires 50Ω characteristic impedance transmission lines and velocity-

matching of the electrical and optical signals. Velocity-matching occurs when the

effective indices of the optical and electrical waveguides are equal. The width, w_c,

strongly affects the impedance, while the thickness, t_c, strongly affects the effective

index. Three sets of calculations were carried out to assign tolerances to the CPW

dimensions for nominal gap widths of 10, 15, and 20 microns respectively. Table 4.3

summarizes the results.
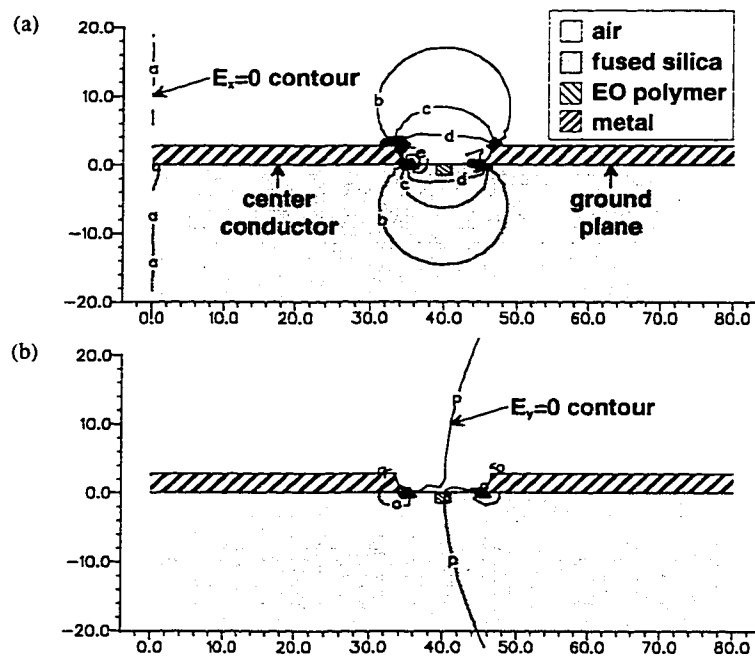
Figure 4.10: Plots of equal field contours resulting from driving the coplanar waveguide as solved by finite element analysis: (a) field in the horizontal direction and (b) field in the vertical direction.

s_c (μm)	w_c (μm)	t_c (μm)	n_{eff}	Z_c (Ω)
10±3	70±3	2.75±0.25	1.520±0.011	52±5
15±3	134±3	2.75±0.25	1.529±0.005	50±2
20±3	185±3	2.75±0.25	1.533±0.006	50±2

Table 4.3: Design results for the CPW electrodes.

4.7. Expected Bandwidth Calculations

There are two mechanisms that determine the theoretical bandwidth (BW) of the devices. First is the degree of velocity-matching which can be achieved. Second is the electrical loss incurred on the CPW (see Appendix A). Table 4.4 shows the results of the expected BW calculations for the different designs of POEMS device to be fabricated. Along with the iterations of gap size, s_c, the length of the CPW, L_c, takes on two values (5 cm and 2.5 cm), and the design wavelength also takes on two values, namely 1.55 μm and 1.32 μm. All of the designs meet the design specification of being able to transmit 10 Gb/s. The calculations in Table 4.4 employ the quasi-static approximation to calculate the electrical effective index and therefore ignore the small effect of increasing frequency on the velocity matching.

s_c nominal (μm)	BW λ=1.55μm		BW λ=1.32μm	
	L_c=5cm (GHz)	L_c=2.5cm (GHz)	L_c=5cm (GHz)	L_c=2.5cm (GHz)
10±3	14*	55*	14*	55*
15±3	41	82	42*	115
20±3	38	76	52	104

Table 4.4: Calculated BW for all of the different designs of POEMS device. L_c is the length of the CPW and * denotes that the limit is due to electrical loss, otherwise the limit is due to velocity-matching.

4.8. Expected Drive Voltage Calculations

The drive voltage required by the modulators is determined by the relative phase difference of the light exiting the two arms of the interferometer given by

$$\Delta\varphi = \frac{4\pi\Delta n_{eff} L}{\lambda_o} \tag{4.9}$$

where Δn_{eff} is the change in the effective index of the optical waveguide given by

$$\Delta n_{eff} = \tfrac{1}{2}\Gamma n_{eff}^3 r_{33} E \tag{4.10}$$

47

where E is the applied electric field and Γ is the confinement factor (the fraction of the optical power that is inside the core of the waveguide). Γ appears in the calculation because only the core of the guide contains EO polymer. The waveguides in the POEMS device have a confinement factor of approximately 85%. In order to switch between the maximum and minimum amplitude level of the output there must be a phase difference of π radians. The voltage required to effect this change is therefore called V_π. Setting $\Delta\varphi$ in (4.9) equal to π and substituting (4.10), the switching voltage-length product can be found as

$$V_\pi \cdot L = \frac{s_c \lambda_o}{2 n_{eff}^3 r_{33} \Gamma} \tag{4.11}$$

where the approximation $E = V / s_c$ has been made. Table 4.5 summarizes the results of this calculation.

E_{poling} (V/micron)	s_c (microns)	L (cm)	V_{poling} (kV)	V_π (V)
100	10	2.5	2.0	24
100	10	5.0	2.0	12
200	10	2.5	4.0	12
200	10	5.0	4.0	6
300	10	2.5	6.0	8
300	10	5.0	6.0	4
100	15	2.5	3.0	36
100	15	5.0	3.0	18
200	15	2.5	6.0	18
200	15	5.0	6.0	9
300	15	2.5	9.0	12
300	15	5.0	9.0	6
100	20	2.5	4.0	48
100	20	5.0	4.0	24
200	20	2.5	8.0	24
200	20	5.0	8.0	12
300	20	2.5	12.0	16
300	20	5.0	12.0	8

Table 4.5: Results of approximate drive voltage calculations as a function of poling field and device length for each different electrode gap size at a wavelength of 1550nm.

4.9. Mask Layout

The photolithography required for the fabrication of the POEMS devices can be split into two layers, one that defines the optical waveguides and a second that defines the metal electrodes. Each of these layers is shown in Figure 4.11 along with the composite structure and the locations of each of the design types. There are a total of 30 devices and 6 test structures on the mask.
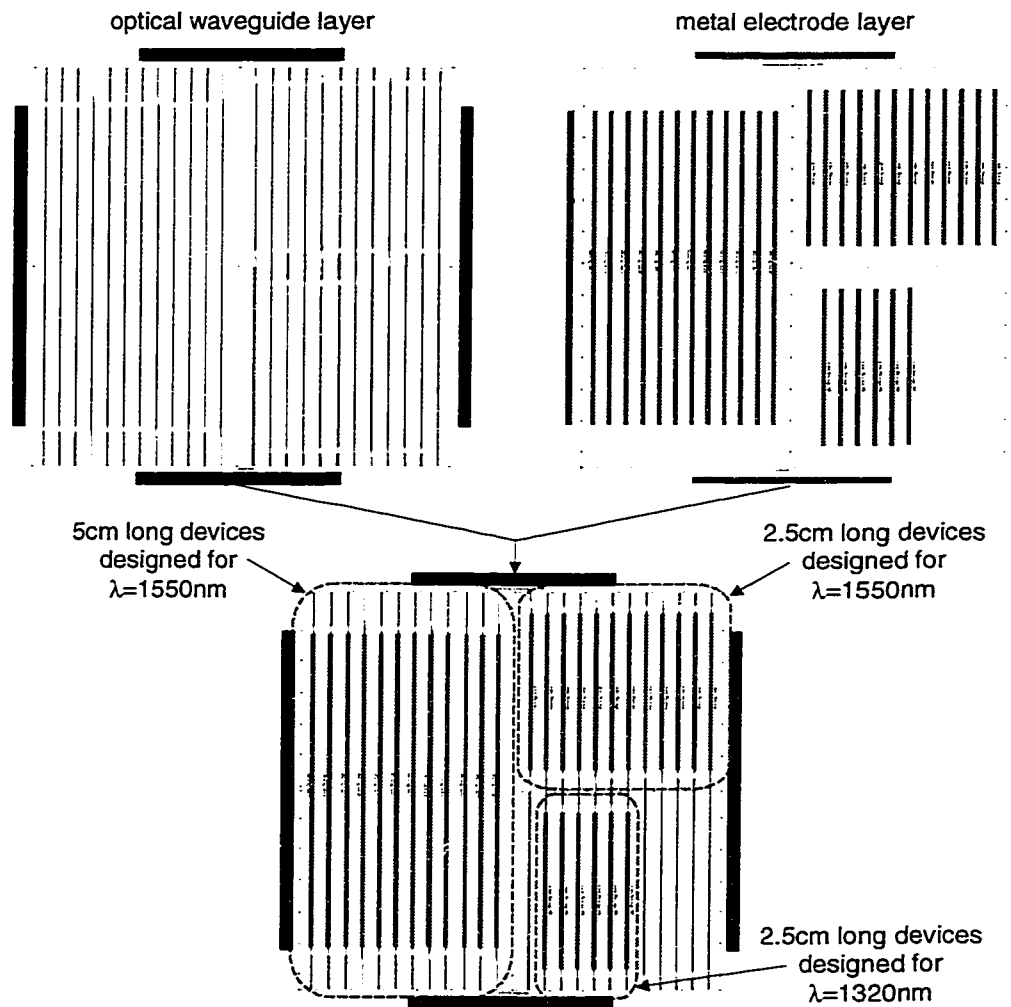
Figure 4.11: The top half of this diagram shows the two layers of the mask set separately. Note that the shaded areas of the optical waveguide mask translate to trenches in the fused silica substrate (the polarity of the actual mask is therefore reversed). The shaded areas of the metal electrode mask translate to metal left behind on the surface.

4.10. Fabrication

The fabrication of the POEMS devices occurs in four phases. Each phase consists of several steps that are detailed in Figure 4.12. Phases 1 and 3 were performed at the Alberta Microelectronics Corporation while phases 2 and 4 were performed at TRLabs.

Phase 1: Etching of Fused Silica Substrate

photolithography using first mask

visual inspection

not in tolerance

checking singlemode guide widths: 2.0±0.2 μm

in tolerance

slow RIE etch of fused silica substrate

profilometer inspection

under etched

checking etch depth: 1.5±0.3 μm

in tolerance

▼ to phase 2

Phase 3: Definition of Metal Electrodes

Au and Cr adhesion layer sputtered onto substrate

surface cleared of all metal

photolithography using second mask

over etched

wet chemical etch of metal layer

under etched

visual inspection

in tolerance

checking distance between bottom of 'cusps': 10.0±3.0 μm

▼ to phase 4

Phase 2: Application of EO Polymer

solution of 250 mg DR1-PMMA per 1 ml Ethyl-L-Lactate Prepared

solution applied to substrate through 0.2μm filter

solution squeegeed onto surface

unacceptable yield

10 minute soft bake at 95°C

excess polymer removed with sharp blade

checking the quality of optical waveguides

acceptable yield

12 hour cure; bake at 120°C

▼ to phase 3

Phase 4: Poling of EO Polymer

substrate submersed in 120°C bath of dielectric fluid

poling field applied

substrate cooled to room temperature with field in place

Figure 4.12: Flow diagram showing the process used to fabricate the POEMS devices.

50

4.10.1 Problems Encountered During Fabrication

During the etching of the fused silica, Phase 1 of the process shown in Figure 4.12, some of the singlemode waveguide sections developed a ripple in their depth which is responsible for high optical loss in the affected guides. The cause of this is unclear but may be due to anisotropy in the substrate material, residual photoresist on the surface or hot-spots during the RIE processing.

Phase 2 requires manual processing of the EO polymer both to apply the polymer solution and to remove the unwanted material. This procedure had to be repeated several times for each sample in order to achieve an acceptable yield. In the end, an average yield of 19 good devices out of 30 was achieved for six substrates. This processing was performed at TRLabs where there are no clean-room facilities available. Contamination of the polymer was therefore a problem. Automation and clean-room facilities could conceivably further increase the yield of this step.

Problems emerged during Phase 3 of fabrication. The first step in this phase is to sputter metal onto the surface of the substrates. The energy of the metal hitting the surface as well as the vacuum needed for sputtering could conceivably damage the EO polymer. Then, during the etching of the metal layer, the polymer is exposed to the metal etchant. Figure 4.13 shows the damage incurred by the EO polymer during this phase of processing. The pinholes and voids in the polymer could be the result of air or solvent trapped in the polymer that leaked out under vacuum. They could also be a result of the exposure to the metal etchant. Cracking and shrinkage could be due to excess solvent left in the polymer or due to thermal stress caused by heating and cooling during and after the sputtering step.
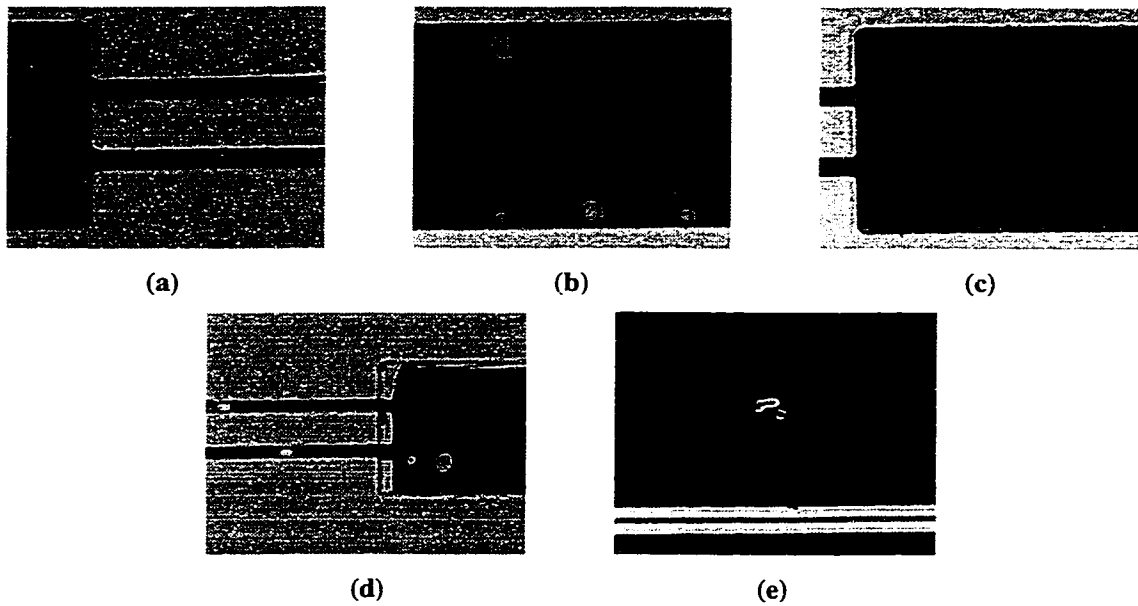
Figure 4.13: Examples of problems encountered during the metalization step, (a) pinholes in the singlemode waveguides, (b) voids in the MMI couplers, (c) cracks in the polymer, (d) shrinkage and (e) liftoff of gold particles over polymer residue.

The main problem in Phase 4 of processing is electrical breakdown and the resulting destruction of otherwise good devices. The cause of the premature breakdown was metal debris in the dielectric fluid. EO polymer residue on the substrates caused poor adhesion of the metal to the surface in small areas. When the substrates were heated to the poling temperature, small bits of metal left the surface and were carried in thermal currents in the dielectric fluid (see Figure 4.13(e)). When one of these particles was observed entering the electrode gap, the resulting disturbance of the field caused dielectric breakdown. To avoid this problem, the substrates were heated to 120°C in the fluid and then cooled without being poled to allow the gold to lift off. The contaminated fluid was then discarded and clean fluid was added to perform the actual poling of the device. To eliminate this problem in the future, the surface of the substrates should be thoroughly cleaned to remove the polymer residue.

Two probes were used to apply the poling field, each attached to one of the ground planes of the CPW. This leaves the center conductor of the CPW to float at a

potential between the two electrode gaps. Imperfections in the electrodes or conductive material in one of the gaps will cause the field to be concentrated in one gap preferentially. This effect lowers the maximum poling field that can be safely applied. In the future, this problem could be alleviated by using three probes instead of two. One of the probes could be connected to the center conductor and the other two to the ground planes. A resistor network could be used to help keep the center conductor at a potential of half that of the applied poling voltage.

4.11. Experimental Results

A visual inspection of all of the devices after fabrication identified only two devices free of obvious defects in the optical waveguides. Both of these devices were 2.5 cm long and designed to have 15 μm gaps between the center conductor of the CPW and the ground planes. The devices were poled using the apparatus shown in Figure 4.14 and characterized using the apparatus shown in Figure 4.15. A close-up of the CPW probes is shown in Figure 4.16. One of the candidate devices was destroyed during poling and the second was poled at a very low voltage to avoid a similar incident.
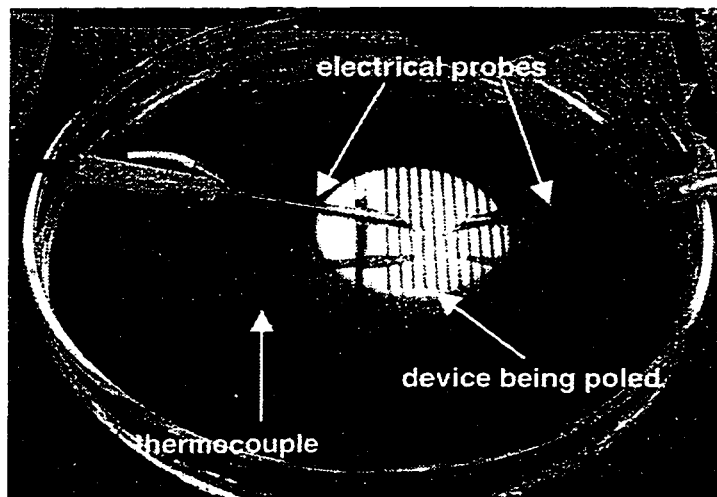
Figure 4.14: The poling station: The devices are poled using two electrical probes attached to the ground planes of the CPW. The devices are submersed in silicone dielectric fluid that is heated to 120°C using a hotplate.

53
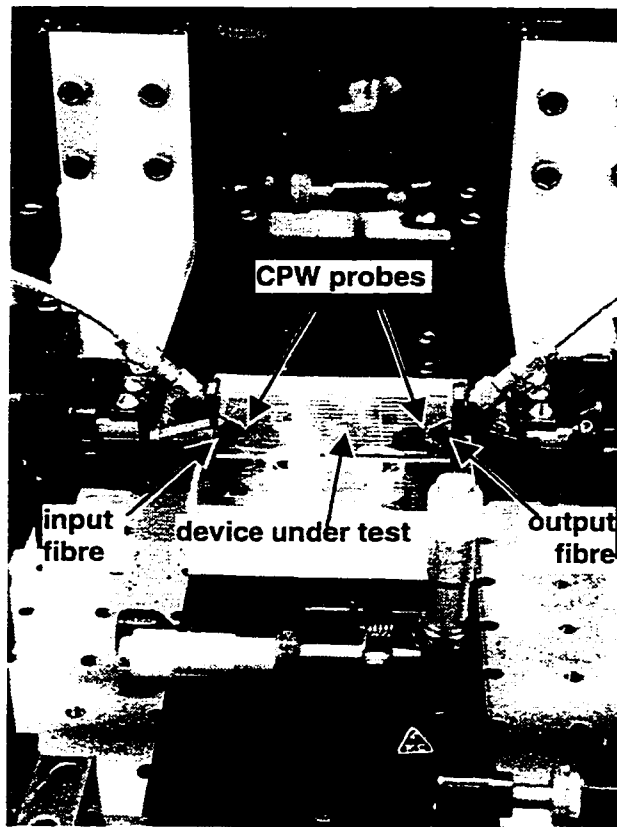
Figure 4.15: The probe station: The electrical probes and optical fibres are moved using 3-axis positioners which are mounted on rails running parallel to the devices. The fibres have two extra axes of tilt for precise alignment to the waveguides. The device under test is placed on a tilt and rotation stage that is mounted on a rail running perpendicular to the devices to facilitate moving from one device to another on the same substrate.
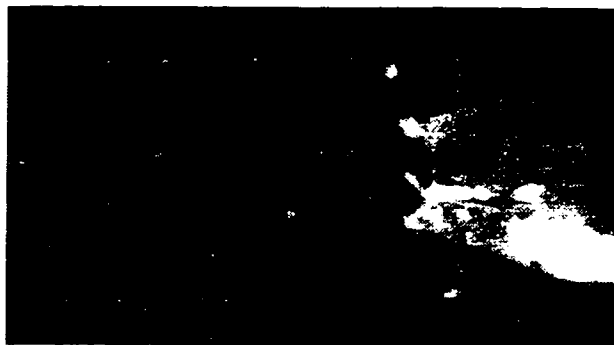
Figure 4.16: Close-up view of a coplanar waveguide probe (at right). These probes have two ground contacts on either side of the center conductor which are brought into contact with the CPW from above the substrate. One probe is used on each end of the CPW in order to launch and terminate the applied signal. The spacing between adjacent probe tips is 150 μm.

4.11.1 Optical Characteristics

All optical waveguide dimensions were within the tolerances specified in the design. The problems during fabrication had destroyed all but a few of the devices and these exhibited high loss due to pinholes in the polymer acting as scattering centers. Another problem for the optics of the POEMS devices was coupling light into and out of the waveguides. The mode of the singlemode sections is very small in comparison to standard singlemode fibre which made butt-coupling difficult and lossy.

Before light could be coupled into the waveguides, suitable end facets had to be created. Several approaches were tried including wafer sawing followed by polishing and cleaving. The polishing was slow and difficult and usually caused the polymer to chip or crack. Cleaving fused silica requires removing a strip of material wider than 1-2 times the thickness of the substrate. It is also difficult to make an accurate scribe mark on the back of the substrate manually. To circumvent these problems, a wafer saw cut was made from the backside of the substrate leaving behind approximately 125 μm of material that could then be easily cleaved.

The optical loss of the single intact device was difficult to deduce. The fibre-to-fibre loss was measured to be 60 dB. Any changes in the average light level while changing the bias voltage could not be resolved by the receiver. The achievable modulation depth was therefore very small. This may have been due to one arm of the Mach Zehnder interferometer having substantially higher loss than the other. Another possibility is that much of the light collected by the output fibre was scattered or uncoupled light and therefore not subject to the EO modulation. In any case, one can only assume that the optical loss of this device was greater than or equal to 60 dB.

4.11.2 Electrical Characteristics

The dimensions of the CPW transmission lines were measured using an optical microscope (for s_c and w_c) and a profilometer (for t_c). The effective index was found by measuring the time delay for pulse propagation through the length of the CPW transmission line using a network analyzer. The results are summarized in Table 4.6.

design values			measured values			target values		calculated values	
s_c (μm)	w_c (μm)	t_c (μm)	s_c (μm)	w_c (μm)	t_c (μm)	n_{eff}	Z_c (Ω)	n_{eff}	Z_c (Ω)
10±3	70±3	2.75±0.25	14.6	62.7	2.26	1.512	52.5	1.515	59.3
15±3	134±3	2.75±0.25	17.5	128	2.26	1.534	49.8	1.524	52.6
20±3	185±3	2.75±0.25	21.8	178	2.26	1.539	49.8	1.540	51.1

Table 4.6: Comparison of measured and calculated transmission line characteristics for the three different device designs.

These devices should meet the design criterion for velocity-matching. To test this, one must first assume a practical minimum bandwidth for a device able to modulate a 10 Gb/s signal, eg. 7 GHz. The bandwidth-length product formula, (A.22), can be rearranged to yield a maximum allowable index difference between the electrical and optical waveguides,

$$\Delta n_{max} = \frac{c}{2.26 BW_{min} L_{max}}$$ (4.12)

where the speed of light, $c = 3 \times 10^8$ m/s, the maximum design length, $L_{max} = 5$ cm and the minimum required bandwidth, $BW_{min} = 7$ GHz. Using these values, $\Delta n_{max} = 0.38$. Adding this to the minimum optical effective index from Table 4.1 gives the maximum allowable effective index of the CPW transmission lines to be 1.85. All of the devices exceed this design criterion for velocity-matching, and therefore have bandwidths suitable to transmit at least 10 Gb/s signals.

A network analyzer was used to measure the forward transmission frequency response, S_{21}, and the reflection characteristics, S_{11}, of the transmission lines. Figure 4.17 shows one of these measurements along with simulations using the measured

dimensions. Electrical loss incurred on the CPW transmission line can limit the modulation bandwidth of a device if it exceeds 6.43 dB (see Appendix A, Section A.2). This device exhibits approximately 2 dB of loss at the maximum measurement frequency of 18 GHz, which would not limit its performance to this point.

The S_{11} curve shows good coupling to the device as it reflects less than -10 dB of the signal throughout the frequency range measured. The notches in this curve arise from multiple reflections at the ends of the transmission line due to the impedance mismatch between the 50 Ω probes and the 59.3 Ω characteristic impedance of the transmission line itself. The frequency positions of these notches depend on the length of the line and the effective index. The agreement between the measurement and simulations indicates that the characteristics of these CPW transmission lines are well understood.

(a)   (b)
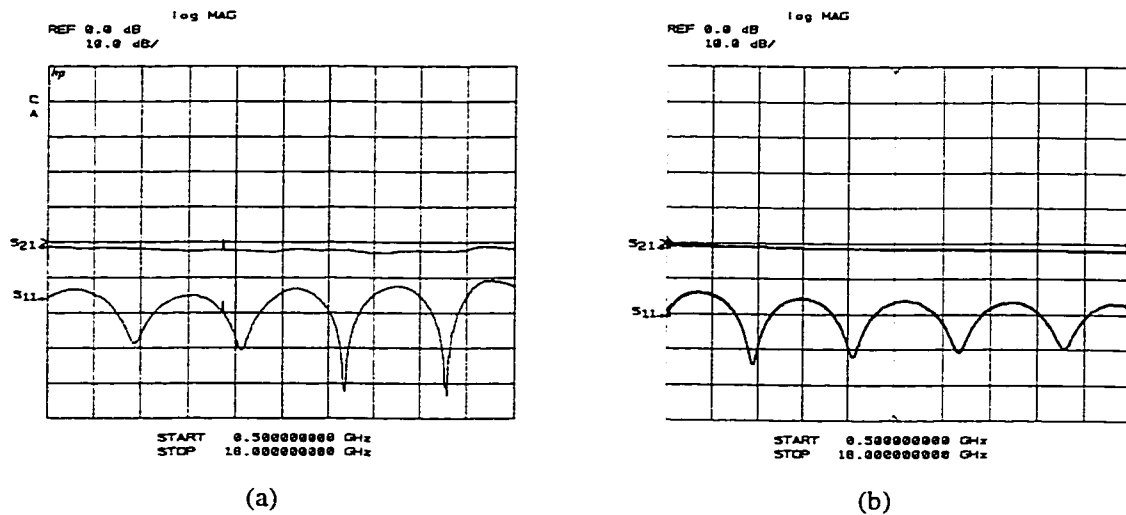
Figure 4.17: (a) Measured frequency response, S_{11} and S_{21}, of a 2.5 cm long CPW transmission line originally designed to have a 10 μm gap and a 70 μm center conductor. The actual dimensions differed due to over-etching, resulting in a 14.6 μm gap and a 62.7 μm center conductor. (b) Simulation shown on the same scale of this transmission line using the measured dimensions.

4.11.3 Modulation Characteristics

Poling of the single working device was performed at the relatively low voltage of 500 V because of the problems discussed in Section 4.10.1. The device was designed to

have CPW dimensions $s_c = (15\pm3)$ µm, $w_c = (134\pm3)$ µm, and $t_c = (2.75\pm0.25)$ µm. The actual dimensions were measured to be $s_c = 23.6$ µm, $w_c = 122$ µm, and $t_c = 2.21$ µm. The optics of the device were designed using y-branches as shown in Figure 4.2; therefore the device had only one input and one output. The half-wave voltage, V_π, of this device was calculated to be 540V using equations (4.2) and (4.11). This high voltage along with the high optical loss incurred in the device necessitated the use of a discrete component biasing circuit and a lock-in amplifier to measure the small modulation signal as shown in Figure 4.18.
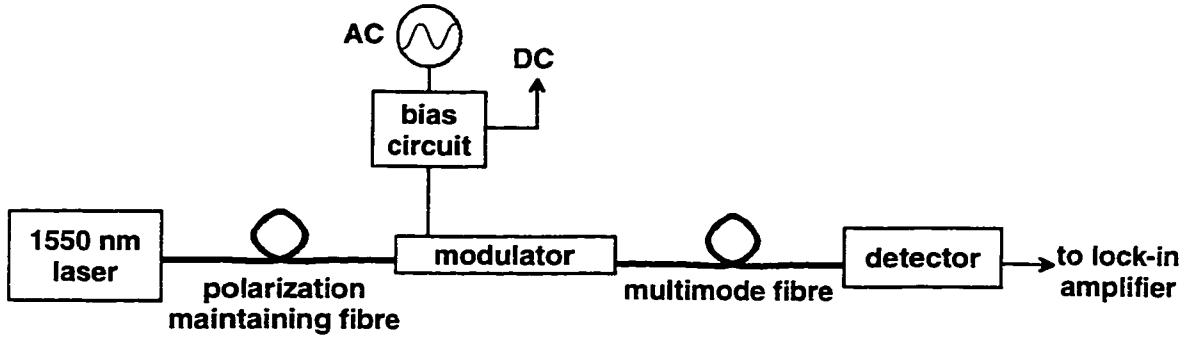
Figure 4.18: Block diagram of the experimental setup used to measure the output optical modulation as a function of the applied bias.

The modulation measurements were performed at a frequency of 1 kHz as the biasing circuit was only able to pass relatively low frequencies. A constant 10 V peak-to-peak modulation was added to the bias voltage that was varied between 0 and 200 V. A constant amplitude light source with a wavelength of 1550 nm was coupled to the input waveguide and the modulated output was collected at the output waveguide.

The modulation output obtained in the experiment can be described in the following way. The transfer function of a Mach-Zehnder interferometer is [59]

$$\frac{I_o}{I_i} \propto \cos^2\left(\frac{\pi V}{2V_\pi}\right)$$

(4.13)

where I_o is the light intensity at the output of the device, I_i is the light intensity at the input of the device and V is the applied voltage. Since the modulation component of the

electrical signal is small compared to V_π, the magnitude optical modulation, $|\delta|$, is approximately proportional to the absolute value of the derivative of this transfer function, i.e.

$$|\delta| = A\left|\sin\left(\frac{\pi V}{V_\pi}\right)\right|$$

(4.14)

where A is an arbitrary magnitude chosen to fit this function to the data. The periodicity of this function provides a means to measure V_π.
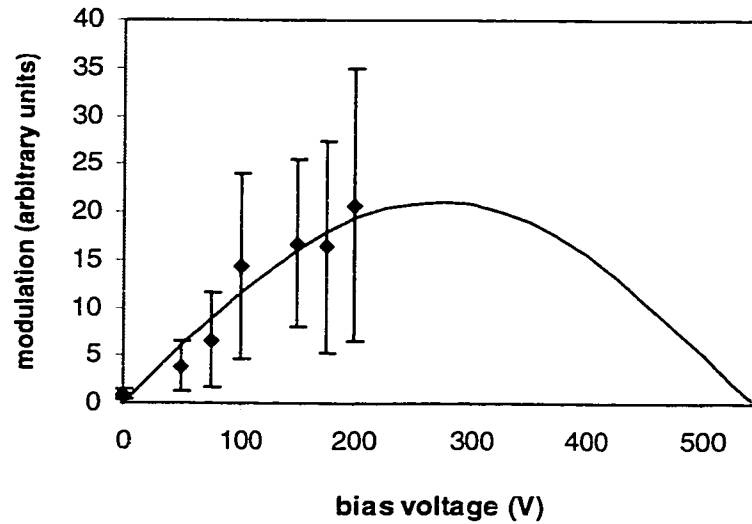
Figure 4.19: Measurements of modulation (points with error bars) and least squares fit (solid line) using the free parameter, A, and fixing the value of $V_\pi = 540$ V as calculated from the poling conditions.

Figure 4.19 shows the results of the modulation measurements along with a theoretical fit using the calculated value of V_π. The signal contained a great deal of noise; therefore multiple measurements were taken at each bias voltage. The average value was then plotted and error bars were derived using ± 1 standard deviation. The data clearly shows an increase in the modulation with increased bias voltage. In order to calculate a value for V_π, points at higher bias voltage would need to be taken to show the periodicity of the curve. Alternatively, if there was less uncertainty in the measurements, a fit to the data could provide an estimate of V_π.

4.12. Discussion

The main problem in the fabrication of the POEMS devices was the damage caused to the EO polymer during the fabrication of the CPW transmission lines. A possible method to prevent this problem would be to add a passivation layer over the EO polymer waveguides. This layer could consist of a durable cross-linked polymer such as a polyimide. The refractive index of this layer could also be chosen to be close to that of the EO polymer thereby increasing the size of the singlemode waveguides. This would further ease fabrication difficulties and facilitate better coupling to singlemode fiber.

An extra polymer layer, as described above, would lower the effective index of the CPW. This could be corrected through the addition of a similar polymer layer over the CPW electrodes, the thickness of which could be varied to ensure velocity-matching. This top layer would also serve as a strong dielectric during poling, eliminating the problems encountered while using a dielectric liquid.

The MMI coupler sections were also problematic during the deposition of the EO polymer. These couplers prohibited the use of spin-coating and etching to fill the trenches defined in the substrates, as the polymer layer would conform to the height variation of the trench in the wide section of the coupler. A possibility to eliminate this problem would be to use integrated waveguide directional couplers instead of MMI couplers. These couplers are constructed using two singlemode waveguides running parallel and close enough together to provide coupling from one guide to the other.

The devices were characterized both electrically and optically. The optical loss was high (≥ 60 dB) and therefore did not meet the design criterion (≤ 6 dB). Electrical measurements yielded results consistent with the calculations used to design the devices. Although modulation measurements could not be done at high frequencies, all indications were that the devices would exceed the design criterion for modulation bandwidth.

5. Conclusions

5.1. The Coordinate Transform Beam Propagation Method

Chapter 2 presented a novel formulation of the BPM for 3D simulations of arbitrarily bent optical waveguides. The algorithm employs a novel split-step Fast Fourier Transform method to apply the propagator, which contains three operators. This method requires little extra computation when compared to the conventional split-step BPM and has the advantage of reducing directly to the conventional split-step BPM for straight propagation. The problem of numerical loss has been solved through a simple renormalization process to ensure power conservation in the computation window. This new method, which includes the complete diffraction term in the out of bend-plane direction, predicts higher bending and transition losses than the earlier IM-BPM, especially for small, singlemode waveguides, which may also have small radii of curvature i.e., less than 1 mm. This method is used subsequently in the design of waveguide bends used in the POEMS device presented in Chapter 4.

5.2. Graded Effective Index Planar Polymer Waveguides

Chapter 3 presented the demonstration and modeling of a novel graded effective index planar polymer waveguide structure. The experimental results and the model are in excellent agreement suggesting that the underlying phenomenon is well understood. The waveguides themselves are easy to fabricate and exhibit low loss. The graded index nature of the structure reduces dispersion compared to multimode step-index waveguides of similar dimensions. This lower dispersion may prove advantageous for application to board-to-board scale interconnects. Applications in coarse WDM and in waveguide optical amplifiers were also presented. Further work has been performed using these waveguides in conjunction with a bulk Erbium/Ytterbium co-doped glass. The resulting

waveguide was able to reach the "break-even" point, i.e., the signal enhancement was enough to overcome the propagation losses in the waveguide. Future work is planned to fabricate graded effective index waveguides and step index waveguides with lengths of one meter for the purpose of experimentally measuring the difference in dispersion between the two structures.

5.3. Polymer Electrooptic Modulator/Switch

Chapter 4 presented the design, fabrication, and testing of a novel electrooptic polymer modulator/switch. The EO polymer used in this device is relatively inexpensive and highly processable in comparison to other crystalline EO materials. The design of the device employs fused silica as the substrate and optical cladding material. The primary advantages of the fused silica are its strength, optical transparency in the near infrared and an electrical permittivity suitable for simple velocity-matching using coplanar transmission lines. A velocity-matched EO polymer device using coplanar transmission lines has not previously been reported. The major disadvantage of the fused silica is the large refractive index difference between it and the EO polymer. This results in the singlemode waveguides being very small and thereby difficult to couple to standard singlemode fibre.

There are two additional advantages of using CPW transmission lines. First is the simple creation of a push-pull device using ground plane-to-ground plane poling. Second is the good control of the transmission line characteristics as the dimensions of the CPW are independent of the polymer deposition.

The experimental characterization of the fabricated devices yielded results that were in agreement with calculated values, thereby validating the approach used in the design of the devices. Modulation measurements were taken using a single device which exhibited a high optical loss (≥ 60 dB). Poling of the device was performed at the

relatively low voltage of 500 V resulting in a half-wave voltage, $V_\pi = 540$ V. The high optical loss along with the high required drive voltage prevented the measurement of the device bandwidth. Electrical measurements suggest that the device would exceed the design criterion for modulation bandwidth, i.e. a bandwidth suitable to transmit a 10 Gb/s signal.

The major problem in the POEMS design is the exposure of the EO polymer to vacuum, metal deposition, and metal etchant during the fabrication of the CPWs. The problem could be alleviated by the addition of a passivation layer covering the surface after the deposition of the EO polymer. A second polymer layer placed over the CPW electrodes could be used to compensate for the reduced effective index of the CPW caused by the passivation layer.

6. References

1. H. S. Hinton and D. A. B. Miller, "Free-Space Photonics in Switching", *AT&T Technical Journal*, pp. 84-92, Jan/Feb 1992.

2. D. W. Boertjes, J. N. McMullin, and B. P Keyworth, "Graded effective index planar polymer waveguides", *J. Lightwave Technol.*, vol. 14, no. 12, pp.2714-2718, 1996.

3. M. D. Feit, J. A. Fleck Jr., "Light propagation in graded-index optical fibers," *Appl. Opt.*, vol. 17, pp. 3990-3998, 1978.

4. P.-C. Lee, E. Voges, "Three-dimensional semi-vectorial wide-angle beam propagation method," *J. Lightwave Technol.*, vol. 12, no. 2, pp. 215-225, 1994.

5. Em E. Kreizis, A. G. Papagiannakis, "A joint finite-difference and FFT full vectorial beam propagation scheme," *J. Lightwave Technol.*, vol. 13, no. 4, pp. 692-700, 1995.

6. G. Ronald Hadley, "Transparent boundary condition for beam propagation," *Opt. Lett.*, vol. 16, no. 9, pp. 624-626, 1991.

7. J. Yamauchi, O. Saito, M. Sekiguchi, H. Nakano, "Polarization dependence of pure bending loss in slab optical waveguides," *IEICE Trans. Electron.*, vol. E79-C, no. 6, pp. 870-873, 1996.

8. T. Gase, L. Erdmann, A. Bräuer, P. Dannberg, W. Karthe, "Polarization-independent phase modulator with electro-optic polymer on a silica substrate for hybrid integration," *OFC '95, 1995 Technical Digest Series*, vol. 8, pp. 282-283, 1995.

9. Henry F. Taylor, "Power loss at directional change in dielectric waveguides," *Appl. Opt.*, vol. 13, no. 3, pp. 642-647, 1974.

10. Mordehai Heiblumm, "Analysis of curved optical waveguides by conformal transformation," *IEEE J. Quantum Electron.*, vol. QE-11, no. 2, pp. 75-83, 1975.

11. R.S. Burton, T.E. Schlesinger, "Semiempirical relation for curved optical waveguide design in the edge-guided mode regime," *J. Lightwave Technol.*, vol. 11, no. 12, pp. 1965-1968, 1993.

12. K. Petermann, "Microbending loss in monomode fibres," *Electron. Lett.*, vol. 12, no. 4, pp. 107-109, 1976.

13. Dietrich Marcuse, "Curvature loss formula for optical fibers," *J. Opt. Soc. Am.*, vol. 66, no. 3, pp. 216-220, 1976.

14. Dietrich Marcuse, "Field deformation and loss caused by curvature of optical fibers," *J. Opt. Soc. Am.*, vol. 66, no. 4, pp. 311-320, 1976.

15. R. Baets, P.E. Lagasse, "Loss calculation and design of arbitrarily curved integrated-optic waveguides," *J. Opt. Soc. Am.*, vol. 73, no. 2, pp. 177-182, 1983.

16. Kwang T. Koai, Pao-Lo Liu, "Modeling of Ti: LiNbO3 waveguide devices: part II - s-shaped channel waveguide bends," *J. Lightwave Technol.*, vol. 7, no. 7, pp. 1016-1022, 1989.

17. J. Yamauchi, S. Kikuchi, T. Hirooka, H. Nakano, "Beam-propagation analysis of bent step-index slab waveguides," *Electron. Lett.*, vol. 26, no. 12, pp. 822-824, 1990.

18. J. Yamauchi, M. Ikegaya, H. Nakano, "BPM analysis of s-shaped dielectric slab waveguides," *Trans. of the IEICE,* vol. 73, no. 11, pp. 1837-1839, 1990.

19. P. Danielsen, D. Yevick, "Propagating beam analysis of bent optical waveguides," *J. Opt. Comm.,* vol. 4, no. 3, pp. 94-98, 1983.

20. A. Maruta, M. Matsuhara, "Analysis of lightwave propagation in a bent waveguide by the Galerkin method," *IEICE Trans. Electron.,* vol. E75-C, no. 6, pp. 736-739, 1992.

21. Michael Rivera, "A finite Difference BPM analysis of bent dielectric waveguides," *J. Lightwave Technol.,* vol. 13, no. 2, pp. 233-238, 1995.

22. J. Saijonmaa, D. Yevick, "Beam-propagation analysis of loss in bent optical waveguides and fibers," *J. Opt. Soc. Am.,* vol. 73, no. 12, pp. 1785-1791, 1983.

23. H. Vendeltorp-Pommer, J. Hedegaard Povlsen, "Bending loss and field distribution in a bent fibre calculated with a beam propagating method," *Opt. Comm.,* vol. 75, no. 1, pp. 25-28, 1990.

24. J. Yamauchi, M. Ikegaya, H. Nakano, "Analysis of bent step-index optical fibres by the beam propagation method," *IEE Proceedings-J,* vol. 139, no. 3, pp. 201-207, 1992.

25. E. Ahlers, R. Pregla, "3-D modelling of concatenations of straight and curved waveguides by MoL-BPM," *Opt. & Quantum Electron.,* vol. 29, no. 2, pp. 151-156, 1996.

26. J. F. Claerbout, *Fundamentals of Geophysical Data Processing: With Applications to Petroleum Prospecting,* New York: McGraw-Hill, Inc., pp. 220-221, 1976.

27. R. T. Chen, H. Lu, D. Robinson, Z. Sun, T. Jannson, D. V. Plant, and H. R. Fetterman, "60 GHz board-to-board optical interconnection using polymer optical busses in conjunction with microprism couplers," *Appl. Phys. Lett.,* vol. 60, no. 5, pp. 536-538, 1992.

28. D. H. Hartman, G. R. Lalk, J. W. Howse, and R. R. Krchnavek, "Radiant cured polymer optical waveguides on printed circuit boards for photonic interconnection use," *Appl. Opt.,* vol. 28, no. 1, pp. 40-47, 1989.

29. R. R. Krchnavek, G. R. Lalk, and D. H. Hartman, "Laser direct writing of channel waveguides using spin-on polymers," *J. Appl. Phys.,* vol. 66, no. 11, pp. 5156-5160, 1989.

30. W. Yu, W. Królikowski, B. Luther-Davies, M. Webster, and M. Austin, "Wave mixing and beam profile control in a photorefractive waveguide," *Opt. Lett.*, vol. 20, no. 6, pp. 563-565, 1995.

31. B. P. Keyworth, J. N. McMullin, R. Narendra, and R. I. MacDonald, "Computer-controlled pressure-dispensed multimode polymer waveguides," *IEEE Transactions CPMT - Part B,* vol. 18, no. 3, pp. 572-577, 1995.

32. B. P. Keyworth, D. J. Corazza, R. I. MacDonald, "Beam extractor card for free-space optical backplanes," *SPIE Proc.*, vol. 2692, Feb. 1996.

33. W. B. Jones Jr., *Introduction to Fiber Communication Systems,* NewYork: Holt, Rinehart and Winston, Inc., pp. 106, 1988.

34. K. Thyagarajan, V. Mahalakshmi, M. R. Shenoy, "Equivalent waveguide model for parabolic index planar segmented waveguides", *Optics Comm.,* vol. 121, part 1/3, pp. 27-30, 1995.

35. R. T. Chen, "Graded index linear and curved polymer channel waveguide arrays for massively parallel optical interconnects," *Appl. Phys. Lett.,* vol. 61, no. 19, pp. 2278-2280, 1992.

36. E. Okuda, I. Tanaka, and T. Yamasaki, "Planar gradient-index glass waveguide and its applications to a 4-port branched circuit and star coupler," *Appl. Opt.,* vol. 23, no. 11, pp. 1745-1748, 1984.

37. N. V. Kuzmina, S. A. Tsyplyaev, "Approximation of the refractive index profile of a planar gradient waveguide under laminar etching.", *Opt. Spectrosc.,* vol. 70, no. 5, pp. 652-654, 1991.

38. C. Ma, S. Liu, "Mode equation and its solution for dielectric waveguide of parabolic cross-section.", *Optical and quantum electronics,* vol. 21, no. 2, pp. 117-122, 1989.

39. D. Gerold and R. T. Chen, "Vacuum-tuned graded-index polymer waveguides on silicon substrates", *Appl. Opt.,* vol. 35, no. 3, pp. 400-403, 1996.

40. Norland Optical Adhesive, no. NOA 81, from Norland Products Inc., Joyce Kilmer Ave., New Brunswick, N. J., 08902.

41. T. Tamir (Ed.), *Guided-Wave Optoelectronics (2nd ed.),* Berlin: Springer-Verlag, Ch. 2, 1990.

42. J. N. McMullin, "Optical circuit board simulations using the propagating beam method," *Proceedings of the First International Workshop on Photonics - Networks, Components & Applications, Montebello, Quebec, Oct. 11-13, 1990,* in Series in Optics and Photonics, vol. t2, Singapore: Word Scientific, pp. 358-362, 1990.

43. M. R. Piaim, C. F. Janz, R. I. MacDonald, and J. N. Broughton, "Compact planar 980/1550nm wavelength multi/demultiplexer based on multimode interference," *IEEE Photon. Technol. Lett.,* vol. 7, no. 10, pp. 1180-1182, 1995.

44. M. Krishnaswamy, D. Boertjes, J. N. McMullin, and B. P Keyworth, "Optical properties of polymer waveguides dispensed on an Erbium/Ytterbium codoped glass", *IEEE J. Selec. Topics Quant. Elec.*, vol. 2, no. 2, pp. 373-377, 1996.

45. Wol-Yon Hwang, Min-Cheol Oh, Hyang-Mok Lee, Heuk Park, and Jang-Joo Kim, "Polymeric 2 x 2 electrooptic switch consisting of asymmetric Y junctions and Mach-Zehnder interferometer", *IEEE Photon. Technol. Lett.*, vol. 9, no. 6, pp. 761-763, 1997.

46. Lucas B. Soldano and Erik C. M. Pennings, "Optical multi-mode interference devices based in self-imaging: principles and applications", *J. Lightwave Technol.*, vol. 13, no. 4, pp. 615-627, 1995.

47. Pierre A. Besse, Marcus Bachmann, H. Melchior, L. B. Soldano, and M. K. Smit, "Optical bandwidth and fabrication tolerances of multimode interference couplers", *J. Lightwave Technol.*, vol. 12, no. 6, pp. 1004-1009, 1994.

48. Srinath Kalluri, Sean Garner Mehrdad Ziari, and William H. Steier, "Simple two-slit interference electro-optic coefficients measurement technique and efficient coplanar electrode poling of polymer thin films", *Appl. Phys. Lett.*, vol. 69, no. 2, pp. 275-277, 1996.

49. H. R. Cho, M. J. Shin, S. H. Han, and J. W. Wu, "Mach-Zehnder interferometer measurement of the Pockels effect in a poled polymer film with a coplanar electrode structure", *Appl. Phys. Lett.*, vol. 69, no. 25, pp. 3788-3790, 1996.

50. K. S. Lee, J. W. Wu M. H. Lee, K. H. Kim, and Y. H. Won, "Measurement of the linear electrooptic effect in poled polymer thin films with coplanar electrodes", *Opt. & Quantum Electron.*, vol. 27, pp. 347-354, 1995.

51. I. Faderl, P. Labeye, P. Gidon, and P. Mottier, "Integration of an electrooptic polymer in an integrated optics circuit on silicon", *J. Lightwave Technol.*, vol. 13, no. 10, pp. 2020-2025, 1995.

52. Graham H. Cross, Yusuf Karakus, and David Bloor, "Electro-optics in thermopoled polymer films", *IEEE Trans. EI*, vol. 28, no. 1, pp. 136-142, 1993.

53. Jung Y. Huang, Chueng L. Liao, Wha T. Whang, and Chi J. Chang , "Thermal stability of second-order nonlinearity in poled polymeric films", *Jpn. J. Appl. Phys.*, vol. 34, part 1, no. 1, pp. 139-144, 1995.

54. R. H. Page, M. C. Jurich, B. Reck, A. Sen, R. J. Twief, J. D. Swalen, G. C. Bjorklund, and C. G. Willson "Electrochromic and optical waveguide studies of corona poled electro-optic polymer films", *J. Opt. Soc. Am. B*, vol. 7, no. 7, pp. 1239-1250, 1990.

55. Jiann T. Lin, Michael A. Hubbard, and Tobin J. Marks , "Poled polymeric nonlinear optical materials. Exceptional second harmonic generation temporal stability of a chromophore-functionalized polyimide", *Chem. Mater.*, vol. 4, no. 6, pp. 1148-1150, 1992.

56. Mark W. Becker, Linda S. Sapochak, Rima Ghosen, Chengzeng Xu, Larry R. Dalton, Yongqiang Shi, William H. Steier, and Alex K.-Y. Jen , "Large and stable nonlinear optical effects observed for a polyimide covalently incorporating a nonlinear optical chromophore", *Chem. Mater.*, vol. 6, no. 2, pp. 104-106, 1994.

57. Min-Cheol Oh and Sang-Yung Shin, "Polymeric polarization-independent modulator incorporating twisted optic-axis waveguide polarization converters", *IEEE Photon. Technol. Lett.*, vol. 8, no. 11, pp. 1483-1485, 1996.

58. Datong Chen, Harold R. Fetterman, Antao Chen, Willian H. Steier, Larry R. Dalton, Wenshen Wang, and Yongquiang Shi, "Demonstration of 110GHz electro-optic polymer modulators", *Appl. Phys. Lett.*, vol. 70, no. 25, pp. 3335-3337, 1997.

59. Bahaa E. A. Saleh and Malvin Carl Teich, *Fundamentals of Photonics*, John Wiley & Sons, Inc., New York, 1991.

60. Toshio Watanabe, Makoto Hikita, Michiyuki Amano, Yoshito Shuto, Satoru Tomaru, "Vertically stacked coupler and serially grafted waveguide: Hybrid waveguide structures formed using an electo-optic polymer", *J. Appl. Phys.*, vol. 83, no. 2, pp. 639-649, 1998.

61. A. Chen, K. Kaviani, A. W. Rempel, S. Kalluri, W. H. Steier, Y. Shi, Z. Liang, and L. R. Dalton, "Optimized oxygen plasma etching of polyurethane-based electro-optic polymer for low loss optical waveguide fabrication", *J. Electrochem. Soc.*, vol. 143, no. 11, pp. 3648-3651, 1996.

62. A. Otomo, G. I. Stegeman, W. H. G. Horsthuis, G. R. Möhlmann, "Strong field, in-plane poling for nonlinear optical devices in highly nonlinear side chain polymers", *Appl. Phys. Lett.*, vol. 65, no. 19, pp. 2389-2391, 1994.

63. K. D. Singer, M. G. Kuzyk, W. R. Holland, J. E. Sohn, S. J. Lalama, R. B. Comizzoli, H. E. Katz, M. L. Schilling, "Electro-optic phase modulation and optical second-harmonic generation in corona poled polymer films", *Appl. Phys. Lett.*, vol. 53, no. 19, pp. 1800-1802, 1988.

64. H. Tang, J. M. Taboada, G. Cao, L. Li, and R. T. Chen, "Enhanced electro-optic coefficient of nonlinear optical polymer using liquid contact poling", *Appl. Phys. Lett.*, vol. 70, no. 5, pp. 538-540, 1997.

65. Thomas A. Tumolillo Jr., Paul R. Ashley, "A novel pulse poling technique for EO polymer waveguide devices using device electrode poling", *IEEE Photon. Technol. Lett.*, vol. 4, no. 2, pp. 142-145, 1992.

66. K. H. Hahn, D. W. Dolfi, R. S. Moshrefzadeh, P. A. Pedersen, C. V. Francis, "Novel two-arm microwave transmission line for high-speed electro-optic polymer modulators", *Electron. Lett.*, vol. 30, no. 15, pp. 1220-1222, 1994.

67. B. C. Wadell, *Transmission line design handbook*, Artech House, Inc., Norwood, MA, 1991

68. Gardiol, *Lossy Transmission Lines*, Artech House, Inc., Norwood, MA, 1987.

69. W. Boyu, X. Guangjun, and J. Xiaomin, "Travelling wave electrode optimisation for high speed electro-optic modulators using the Fourier series method", *IEE Proc.-Optoelectron.*, vol. 141, no. 6, pp. 381-390, 1994.

Appendix A. Bandwidth-Length Product Calculations

This appendix presents the basic theory necessary to calculate the bandwidth-length product of a travelling wave Mach-Zehnder interferometer. There are two contributions that limit bandwidth, namely velocity-matching and electrical loss. Each of these will be treated separately in the following sections.

A.1. Velocity-matching Considerations

The purpose of this section is to find the electrical -3dB bandwidth–length product of a travelling wave Mach-Zehnder interferometer in the absence of any electrical loss on the driving electrode(s). Figure A.1 shows a schematic representation of the interaction of the optical and electrical signals on one arm of an interferometer.
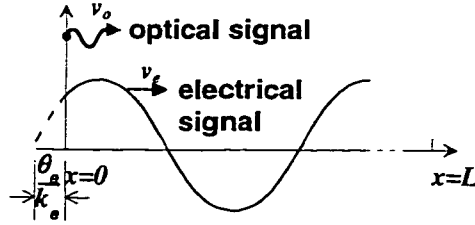

Figure A.1: Schematic diagram of the interaction of light and the electrical signal on one arm of a Mach-Zehnder interferometer. The arm is of length L. Both signals start at $x=0$ at $t=0$ and propagate to $x=L$ with their respective velocities.

The optical signal moves with a velocity v_o and the electrical signal is assumed to be a sine wave, with a velocity v_e, of the form

$$E = E_o \sin(k_e x - \omega_e t + \theta_e) \qquad (A.1)$$

where E_o is the maximum field strength, k_e is the electrical propagation constant, ω_e is the radial frequency and θ_e is an arbitrary phase constant. The velocity of both waves is related to their effective indices through

$$v_o = c / n_{opt} \qquad (A.2a)$$

$$v_e = c / n_{elec} \qquad (A.2b)$$

where c is the speed of light, n_{opt} and n_{elec} are the optical and electrical effective indices respectively.

Using the EO index change given in (4.1b), the phase change of the light travelling through this arm of the interferometer relative to the base phase change when no field is applied can be found as

$$\Delta\varphi = \int_0^L dx \frac{\pi r_{33} n_{opt}^3 E_o}{\lambda_o} \sin(k_e x - \omega_e t + \theta_e) \qquad (A.3)$$

where the integration variable, x, is made to follow the optical signal, thereby sampling the electric field in the same way. Therefore, let

$$x = v_o t \qquad (A.4)$$

and, for simplicity, let

$$B = \frac{\pi r_{33} n_{opt}^3 E_o}{\lambda_o}. \qquad (A.5)$$

Although n_{opt} and consequently v_o are functions of E, their change due to the EO effect is much smaller than the allowable difference between n_{opt} and n_{elec} for velocity-matching. Therefore, n_{opt} will be considered to be a constant. Substituting (A.4) and (A.5) into (A.3)

$$\Delta\varphi = B v_o \int_0^{t_1} dt \sin(k_e v_o t - \omega_e t + \theta_e). \qquad (A.6)$$

Using that $t_1 = n_{opt} L / c$ and $k_e = \omega_e n_{elec} / c$, the above integration can be performed giving

$$\Delta\varphi = \frac{Bc}{\Delta n \omega_e} \left[\cos\theta_e - \cos\left(\frac{\Delta n \omega_e L}{c} + \theta_e \right) \right] \qquad (A.7)$$

where $\Delta n = n_{elec} - n_{opt}$ and the assumption has been made that $n_{elec} > n_{opt}$, which is true for all cases of interest for the POEMS device.

71

Since it is the maximum phase change that is of interest for calculating the modulation bandwidth, θ_e will be chosen accordingly. The maximum effect is achieved when the light passes through the peak of the electrical signal symmetrically, i.e.

$$\theta_e = \frac{\pi}{2} - \frac{1}{2}\left(\frac{\Delta n \omega_e L}{c}\right),\qquad\text{(A.8)}$$

which gives the maximum phase change as

$$\Delta\varphi_{max} = \frac{2Bc}{\Delta n \omega_e}\sin\left(\frac{\Delta n \omega_e L}{2c}\right).\qquad\text{(A.9)}$$

This is a decaying cyclic function of frequency, having a maximum value at $\omega_e = 0$.

Now the problem is to find the electrical-out response of the interferometer to a sinusoidally varying phase change for small signals. The small signal analysis gives the worst case bandwidth for a Mach-Zehnder. Biasing the interferometer at the half-power point, let

$$\Delta\varphi = \frac{\pi}{2} + A\frac{\pi}{2}\sin\omega_e t\qquad\text{(A.10)}$$

where

$$A \ll 1\qquad\text{(A.11)}$$

and A is determined from $\Delta\varphi_{max}$. The light intensity output of a Mach-Zehnder interferometer is [59]

$$I_o = I_i \cos^2(\Delta\varphi/2)\qquad\text{(A.12)}$$

where I_i is the light intensity at the input and I_o is the modulated light output (ignoring any constant loss in the waveguide structure). The current in a photodetector is proportional to I_o, and, for the calculation of bandwidth, only relative differences in current are important, thus one can ignore any proportionality constants, i.e., let

$$I_e = \frac{1}{2}\cos\Delta\varphi\qquad\text{(A.13)}$$

where I_e is the current where the DC portion of the current has been subtracted off. The average electrical power in the receiver is proportional to the square of the current and can be found from (once again ignoring proportionality constants)

$$\overline{P} = \frac{1}{\tau} \int_0^\tau dt \, I_e^2 \tag{A.14}$$

where $\tau = 2\pi / \omega_e$ is the period of the electrical signal. Then substituting (A.13) and (A.10) gives

$$\overline{P} = \frac{1}{4\tau} \int_0^\tau dt \sin^2\left(\frac{A\pi}{2} \sin \omega t\right). \tag{A.15}$$

For small signal analysis, $\sin x \rightarrow x$, giving

$$\overline{P} = \frac{A^2 \pi^2}{16\tau} \int_0^\tau dt \sin^2 \omega t. \tag{A.16}$$

Now the integration can be performed resulting in

$$\overline{P} = \frac{A^2 \pi^2}{32}, \tag{A.17}$$

therefore, $\overline{P} \propto A^2$. Thus, the -3dB modulation point occurs when A falls to $1/\sqrt{2}$ of its maximum value and since $A \propto \Delta\varphi_{max}$, the -3dB point can be expressed in terms of the phase change as

$$\Delta\varphi_{max}(\omega = 2\pi BW) = \frac{1}{\sqrt{2}} \Delta\varphi_{max}(\omega = 0) \tag{A.18}$$

which can be rewritten as

$$\frac{\Delta n \pi BW \cdot L}{\sqrt{2}c} - \sin\left(\frac{\Delta n \pi BW \cdot L}{c}\right) = 0 \tag{A.19}$$

where the solution will be taken to be the first positive root of this equation. For simplicity, let

$$V = \frac{\Delta n \pi BW \cdot L}{c} \tag{A.20}$$

73

then the equation is

$$\frac{V}{\sqrt{2}} - \sin V = 0 \tag{A.21}$$

for which the solution is (approximately) $V = 1.39$. The bandwidth-length product from (A.20) is then

$$BW \cdot L = \frac{c}{2.26\Delta n}. \tag{A.22}$$

A.2. Electrical Loss Considerations

The frequency dependent electrical loss on a CPW contributes to the limitation of the bandwidth-length product of a Mach-Zehnder interferometer by decreasing the phase modulation of the exiting light. This loss arises from two different sources, namely, material losses (both conductors and dielectrics) and radiation losses due to the waveguide structure itself. Both of these losses increase with increasing frequency and produce a long, slow roll-off in the modulation efficiency. The form of the loss is difficult to find analytically, therefore, a loss per unit length was solved for at selected frequencies using a microwave structure simulation package called MDS. Table A.1 shows the values of the material properties used in these simulations.

Material Property	value	unit
conductivity of gold	4×10^7	S
loss tangent of fused silica	0.0002	
relative permittivity of fused silica	3.823	
thickness of substrate	1500	μm

Table A.1: Values of the material properties used in MDS simulations.

Once again, it is convenient to start with the EO index shift given in equation (4.1b) to get the relative phase change of light exiting one arm of an interferometer (of length L)

$$\Delta\varphi = \frac{\pi r_{33} n_{opt}^3}{\lambda_o} \int_o^L dx E(x) \tag{A.23}$$

74

where the integral generalizes the equation to allow for an electric field which decays as a function of the distance along the line. The peak electric field has the form

$$E_{peak}(x) = E_o \exp(-\alpha_e x).$$ (A.24)

Integrating (A.23) after substituting (A.24) gives

$$\Delta\varphi_{max} = \frac{\pi r_{33} n_{opt}^3 E_o}{\lambda_o \alpha_e}[1 - \exp(-\alpha_e L)]$$ (A.25)

which is a decaying function of frequency (implicitly through α_e) having a maximum at $\omega_e = 0$ where no loss is incurred (i.e. $\alpha_e = 0$). Taking the limit of the above expression as $\alpha_e \to 0$ gives

$$\Delta\varphi_{max}(\omega_e = 0) = \frac{\pi r_{33} n_{opt}^3 E_o L}{\lambda_o}$$ (A.26)

Then using (A.18) to find the -3dB modulation point one arrives at the following equation

$$\frac{\alpha_e L}{\sqrt{2}} - 1 + \exp(-\alpha_e L) = 0$$ (A.27)

the non-trivial solution of which is (in Nepers)

$$\alpha_e L = 0.738 \, \text{Np}.$$ (A.28)

Converting this to decibels, keeping in mind that the above describes the decay of electric field, gives the maximum loss allowable on a CPW electrode resulting in the half power modulation point as

$$\text{maximum loss} = 6.43 \text{ dB}.$$ (A.29)